Circadian control of DRP1 activity regulates mitochondrial dynamics and bioenergetics

Authors: Karen Schmitt[1,2,&], Amandine Grimm[1,2,&], Robert Dallmann[3], Bjoern Oettinghaus[4], Lisa Michelle Restelli[4], Melissa Witzig[1,2], Naotada Ishihara[5], Katsuyoshi Mihara[6], Jürgen A Ripperger[7], Urs Albrecht[7], Stephan Frank[4#], Steven A. Brown[3*#], Anne Eckert[1,2,8*#]

Affiliations:

[1]Neurobiology Lab for Brain Aging and Mental Health, Transfaculty Research Platform, Molecular & Cognitive Neuroscience, University of Basel, Basel, Switzerland

[2]Psychiatric University Clinics, University of Basel, Basel, Switzerland

[3]Chronobiology and Sleep Research Group, Institute of Pharmacology and Toxicology, University of Zurich, Zurich, Switzerland

[4]Division of Neuropathology, Institute of Pathology, University Hospital Basel, Basel, Switzerland

[5]Department of Protein Biochemistry, Institute of Life Science, Kurume University, Kurume 839-0864, Japan

[6]Department of Molecular Biology, Graduate School of Medical Science, Kyushu University, Fukuoka 812-8582, Japan

[7]Department of Biology, Unit of Biochemistry, University of Fribourg, Fribourg, Switzerland

[8]Lead contact

Correspondence:

*To whom correspondence may be addressed: E-mail: steven.brown@pharma.uzh.ch or anne.eckert@upkbs.ch.

[&]These authors equally contributed.

[#]Senior authors.

Highlights:

- The circadian clock controls rhythmic mitochondrial dynamics and metabolic flux.
- DRP1 is phosphorylated in circadian fashion.
- Suppression of DRP1 activity eliminates circadian ATP production.
- Blocking DRP1 function impairs the core circadian clock.

eTOC Blurb/ In Brief:

Schmitt et al. demonstrate that the circadian clock globally regulates mitochondrial morphology and energy metabolism. Even in non-dividing tissues, rhythmic control of DRP1 phosphorylation directs circadian mitochondrial morphology. This control is not only essential for circadian ATP production, but also feeds back to influence the core circadian clock.

Summary

Mitochondrial fission-fusion dynamics and mitochondrial bioenergetics, including oxidative phosphorylation and generation of ATP, are strongly clock-controlled. Here we show that these circadian oscillations depend on circadian modification of Dynamin-related Protein 1 (DRP1), a key mediator of mitochondrial fission. We used a combination of in vitro and in vivo models, including human skin fibroblasts and DRP1-deficient or clock-deficient mice, to show that these dynamics are clock-controlled via circadian regulation of DRP1. Genetic or pharmacological abrogation of DRP1 activity abolished circadian network dynamics and mitochondrial respiratory activity, and eliminated circadian ATP production. Pharmacological silencing of pathways regulating circadian metabolism and mitochondrial function (e.g. sirtuins, AMPK) also altered DRP1 phosphorylation, and abrogation of DRP1 activity impaired circadian function. Our findings provide new insight into the crosstalk between the mitochondrial network and circadian cycles.

Keywords

Bioenergetics; circadian clock; DRP1; dynamics; fission, fusion, glycolysis, metabolism, mitochondria, oxidative phosphorylation.

Introduction

The circadian clock is a hierarchical network of oscillators that synchronize a wide variety of metabolic pathways to the optimal time of day, anticipating periodic changes of the external environment for all living organisms, from cyanobacteria and fungi (Brunner and Schafmeier, 2006) to insects (Rosato et al., 2006) and mammals (Gachon et al., 2004).

Over the years, a growing body of evidence has emerged specifically suggesting that energy metabolism and cellular antioxidant mechanisms defending against oxidative damages are coordinated by the circadian clock. Conversely, disruption of the clock impairs metabolic homeostasis (McGinnis and Young, 2016). The circadian clock exerts its control over metabolism by (i) controlling the expression of genes and enzymes involved in metabolic processes (Eckel-Mahan et al., 2012, Feng et al., 2011, Vollmers et al., 2009), (ii) intertwining nuclear receptors and nutrient sensors with the clock machinery, e.g. PER2/CLOCK and SIRT1 (Asher et al., 2008, Nakahata et al., 2008); PER2 and PPARα/REV-ERBα (Schmutz et al., 2010), CRY1 and AMPK/GCR (Lamia et al., 2011, Lamia et al., 2009); and REV-ERBα and HDAC3 (Zhang et al., 2015), and/ or (iii) regulating metabolite levels (e.g. NAD^+/NADH; ATP/ADP; cAMP) (Nakahata et al., 2009, O'Neill et al., 2008, Peek et al., 2013, Ramsey et al., 2009). Conversely, various hormones, nutrient and redox sensors as well as metabolites not only act as clock output but can, in turn, also regulate the biological clock by acting as input signals (Bass, 2012, Eckel-Mahan and Sassone-Corsi, 2013).

Within this network, the mechanistic relationship between the clock and the mitochondrial network remains mostly elusive. Mitochondria are highly dynamic cellular organelles playing a major role in cellular energy metabolism and homeostasis via generation of several metabolites including adenosine triphosphate (ATP). Several studies have shown diurnal oscillations not only in mitochondrial gene expression (Panda et al., 2002), but also in key mitochondrial bioenergetic parameters including membrane potential, cytochrome c oxidase

activity and key mitochondrial enzymes (Isobe et al., 2011, Neufeld-Cohen et al., 2016). Moreover, one regulatory node for mitochondrial oxidative metabolism is the level of NAD^+/NADH, which regulates the activity of mitochondrial sirtuins and thereby mitochondrial protein acetylation (Nakahata et al., 2009, Peek et al., 2013, Masri et al., 2013). However, in other systems such as the cell cycle, global control of mitochondrial function is strongly coordinated with morphology (Lopez-Mejia and Fajas, 2015, Wai and Langer, 2016). For example, in response to cues from the cell cycle, a tightly regulated equilibrium between opposing mitochondrial fusion and fission activities is required to meet changing demands for energy production and to adjust mitochondrial function (Kanfer and Kornmann, 2016). In this paper, we show that similar mechanisms are used by the circadian clock to regulate the mitochondrial network: even in non-dividing cells and tissues, circadian regulation of dynamin-related protein 1 (DRP1) results in cycles of fission and fusion that are essential for circadian oscillations in ATP production. Our findings are consistent with the existence of a crosstalk between the clock and the mitochondrial network that maintains bioenergetic homeostasis in response to circadian metabolic changes.

Results & Discussion

Cellular bioenergetic variations are driven by the circadian clock.

To eliminate potential systemic and environmental influences upon metabolic measurements and to establish an *in vitro* system for mechanistic study, global metabolomic profiles were first obtained from cultured human osteosarcoma U2OS cells over the course of 24 hours after synchronizing circadian clocks with dexamethasone **(Fig 1A-C, Fig S1A-E, Table 1)**. Similar to circadian pathway signatures of the cellular metabolome previously described in rodents (Eckel-Mahan et al., 2012, Minami et al., 2009, Adamovich et al., 2014, Vollmers et al., 2009) and humans (Ang et al., 2012, Dallmann et al., 2012, Davies et al., 2014, Kasukawa et al., 2012), periodic analysis (Hughes et al., 2010) showed that ~29% of these metabolites (67 of 228 identified metabolites) displayed circadian rhythmicity, mainly peaking at 16 hours after synchronization (**Fig 1A-C, Fig S1A-E, Table 1**). A range of these rhythmic compounds were engaged in redox and mitochondrial energetic homeostasis through branched-chain amino acid metabolism, the GSH/GSSG redox system, glycolysis, the tricarboxylic acid (TCA) cycle (Fig S1 B-E), or metabolic byproducts of mitochondrial metabolism (i.e. ATP, reactive oxygen species and NAD^+/NADH) (**Fig. S1F-I**), as has been observed by others in heterologous mammalian systems (Eckel-Mahan et al., 2012, Peek et al., 2013). The group of mitochondrial fuels showed peak expression levels about six hours earlier than the "byproduct" group. In fibroblasts from *mPer1/Per2* mutant mice, which lack a functional circadian clock (Zheng et al., 2001),ATP levels remain constant at nadir levels (**Fig 1D**). Thus, rhythmic ATP levels depend upon a functional circadian clock.

Since the circadian clock can be phase-locked with the cell cycle (Matsuo et al., 2003), and ATP levels are cell cycle-regulated (Marcussen and Larsen, 1996), we also verified ATP content in synchronized fibroblasts treated with cytosine β-D-arabinofuranoside (AraC) to abrogate cell division (**Fig. S2A-C**). Although disruption of cell division with AraC led to a

moderately decreased rhythmic ATP content (**Fig. S2B**), no alteration in the amplitude of circadian ATP production was observed (**Fig. S2A, C**). Circadian ATP levels as well as circadian NAD^+ and NADH levels were also observed in adult wild-type mouse brains, where dividing cells represent a small minority (**Fig. S2D-F**).

Finally, to confirm that this rhythmicity was dependent upon mitochondrial oxidative phosphorylation (OxPhos) rather than glycolysis, we also monitored ATP content in synchronized fibroblasts in the presence of oligomycin, an ATP synthase inhibitor, or 2-deoxy-glucose, a glycolysis inhibitor, to determine the relative contribution of each pathway to the observed ATP oscillations (**Fig. 1E**). Whereas circadian ATP oscillations were significantly dampened by oligomycin treatment, 2-deoxy-glucose only decreased ATP levels while rhythmicity was maintained, confirming that circadian ATP rhythmicity is primarily caused by mitochondrial OxPhos. Collectively, these data not only confirm that mitochondrial output is circadian and cell cycle-independent, but that circadian control likely affects multiple steps of mitochondrial oxidative phosphorylation. We therefore began to dissect the sources of this control.

Circadian mitochondrial bioenergetics are coupled to circadian mitochondrial architecture.

Previous studies have suggested circadian bioenergetics in both SCN and liver (Isobe et al., 2011, Peek et al., 2013). Similarly, in cultured fibroblasts mitochondrial oxygen consumption analyses showed time-of-day-dependent variation in each measurable step of the mitochondrial respiratory chain: at 16 hours post-synchronization in cultured cells (and during the mouse subjective day), cells exhibited a higher respiratory capacity corresponding to high ATP levels; and at 28 hours post-synchronization (during the subjective night), cells showed lower spare respiratory capacity corresponding to low ATP levels (**Fig 1F, G**). By contrast, oxygen consumption allocated to other sources such as proton leak, or glycolysis (as reflected by the

extracellular acidification rate, or ECAR) remained unchanged at different time points (**Fig. S2G, H**). Thus, in cultured cells only mitochondrial respiration, but not glycolysis, varied in a circadian manner by switching between metabolically active and resting states, corresponding to 16 and 28 hours post-shock, respectively (**Fig. 1H**).

Circadian oscillations of mitochondrial function might be explained by a variety of mechanisms (Manella and Asher, 2016). It is formally possible that circadian control of expression of a key rate-limiting mitochondrial enzyme would be sufficient (Neufeld-Cohen et al., 2016). We observed that mitochondrial subunits of complexes I, IV, and V were expressed in a circadian fashion in human fibroblasts (**Fig. S4A**). However, it is unlikely that these variations would create circadian oscillations at each step of the respiratory chain. A second more persuasive idea is that circadian control of NAD^+/NADH levels feeds back to control mitochondrial output (Asher and Schibler, 2011, Nakahata et al., 2009, Peek et al., 2013). Recently, it has been shown that changed in NAD^+/NADH levels can affect activity of the mitochondrial deacetylase SIRT3, thereby affecting global mitochondrial protein acetylation (Peek et al., 2013). A third idea relates to mitochondrial morphology: for example, in the case of the cell cycle, direct regulation of mitochondrial morphology itself regulates all aspects of oxidative respiration (Mishra and Chan, 2014, Westermann, 2010).

Mitochondria are highly mobile, dynamic organelles that continuously fuse and divide, thereby up- or downregulating respiration in response to cellular energy requirements (Wai and Langer, 2016). To investigate whether the circadian clock intervenes globally in mitochondrial dynamics, we assessed mitochondrial morphology in synchronized cultured fibroblasts by confocal microscopy (**Fig. 2A, B**). Matching the rhythmicity in ATP content and OxPhos activity (**Fig. 1**), we observed that mitochondrial network morphology displayed a circadian rhythmicity with three distinct states: tubular at 16 hours, intermediate at 20-24 hours, and fragmented at 28 hours post-shock (**Fig. 2E, Fig. S2I-P**). Similar results were obtained in

another circadian-rhythmic human cell line, glioma A172 (**Fig. S3A-H, J**) as well as in histological sections of hippocampus **(Fig. 2C, F)** and liver (**Fig. S3 I, K**) from wild-type mice, which both displayed a tubular morphology at CT0 (onset of subjective day or rest period) and a fragmented state CT12 (onset of subjective night or activity period). A fragmented mitochondrial network was detected at both time points in the hippocampus of *mPer1/Per2* double mutant mice (**Fig. 2C, D**), as might be expected from their low and constant ATP levels.

Clock control of DRP1 activity modulates circadian mitochondrial metabolism.

A well-defined set of proteins regulates mitochondrial fission and fusion, including mitofusins and dynamin-related proteins. Whereas a recent study suggested circadian oscillation of these genes at a transcriptional level in liver (Jacobi et al., 2015), their expression levels did not exhibit circadian oscillations in cultured cells (**Fig. S4B**). However, we found circadian oscillations in the transcription of other mitochondrial genes encoding complex I, IV, and V subunits (**Fig. S4A**). This disparity of results across experimental systems implied that the 24-hour oscillations in mitochondrial network architecture could be controlled by another mechanism. At the proteome level, it has been shown that the abundance of many key mitochondrial enzymes vary with time of day in clock-dependent fashion, including those whose transcription did not (Neufeld-Cohen et al., 2016), suggesting a possible post-transcriptional mechanism.

In the context of the cell cycle, oscillations in mitochondrial dynamics are regulated via phosphorylation and activation/inactivation of DRP1 by kinases and phosphatases (reviewed by (Otera et al., 2013). The elongation of mitochondria is the direct consequence of the PKA-mediated DRP1 phosphorylation at serine residue 637 (Ser637), which inhibits intra-molecular DRP1 interactions between its GTPase and GED domains, thereby impinging on DRP1 GTPase activity and function (Cereghetti et al., 2008, Cribbs and Strack, 2007, Chang and Blackstone, 2007). This mechanism has been shown previously to be of importance during starvation to

protect starving cells from autophagy (Gomes et al., 2011). In opposition to PKA-mediated DRP1 phosphorylation at the key Ser637, the activation of calcineurin, which is regulated by the circadian clock (Huang et al., 2012), dephosphorylates DRP1 at Ser637 and consequently leads to organelle fragmentation by boosting DRP1 translocation to mitochondria (Cereghetti et al., 2008, Wang et al., 2011).

Thus, we next considered a potential contribution of the biological clock in the post-translational modification of DRP1 by phosphorylation at Ser637 (**Fig. 3**). While total DRP1 protein did not display circadian oscillation both in cell (**Fig. 3A**) and brain lysates of wild-type mice maintained in constant darkness (**Fig. 3B**), Ser637 phosphorylated DRP1 levels exhibited 24-hour rhythms coinciding directly with a fused mitochondrial network with peaks occurring at 20 hours post-shock and at CT12 (onset of the subjective night), respectively. By contrast, when brain lysates from *mPer1/mPer2* double mutant mice were investigated, Ser637 phosphorylated DRP1 levels remained unchanged between CT0 and CT12 (**Fig. 3C**).

We next investigated possible sources for regulation of DRP1 phosphorylation. We therefore evaluated the impact of pharmacological inhibition of calcineurin on DRP1 in synchronized human primary skin fibroblasts (**Fig. 3D**). We observed a significantly increased Ser637-phosphorylation of DRP1 at all time points in the presence of calcineurin inhibitor FK506, resulting in abrogation of its circadian phosphorylation pattern.

Multiple previous studies have suggested diverse methods of feedback from the circadian clock to oxidative metabolism, notably via the nutrient sensors AMPK (Lamia et al., 2009), SIRT1 (Asher et al., 2008, Nakahata et al., 2008), and SIRT3 (Peek et al., 2013). To elucidate whether these control nodes also impact the circadian control of DRP1 phosphorylation, we inhibited circadian-connected nutrient sensors AMPK, SIRT1, and SIRT3 using compound C (Oosterman and Belsham, 2016), Ex527 (Gertz et al., 2013), and AGK7 (Outeiro et al., 2007), respectively, in synchronized human primary skin fibroblasts (**Fig. 3E-G**). In all three scenarios,

Ser637-phosphorylated DRP1 did not exhibit circadian oscillations after respective inhibitor treatments. Taken together, these results not only suggest that mitochondrial network remodeling *in vitro* and *in vivo* is controlled by the circadian clock, but they also indicate that DRP1 phosphorylation could play a central role in nutrient sensor-modulated circadian control of mitochondrial function.

Finally, to determine whether circadian modulation of DRP1-dependent mitochondrial dynamics is indeed responsible for circadian mitochondrial output, we first took a pharmacological approach, treating clock-synchronized cells with P110, a specific mitochondrial division inhibitor (Qi et al., 2013). Treatment with this drug completely abolished circadian ATP variation in human skin fibroblasts (**Fig. 4A**). Similar results were observed in presence of Mdivi-1, formerly reported as a specific inhibitor of DRP1-dependent fission (Bordt et al., 2017) (**Fig S4C**). To further confirm whether inhibition or absence of DRP1 is able to impact ATP oscillation, we evaluated ATP content in *Drp1*$^{-/-}$ MEFs, and found that cells lacking DRP1 did not display ATP oscillations (**Fig. 4B**). To further verify the role of DRP1 in controlling circadian ATP levels *in vivo*, we examined hippocampi of adult *Drp1*$^{-/-}$ mice (Oettinghaus et al., 2016) kept in constant darkness (**Fig. 4C**). Consistent with our *in vitro* observations, ATP levels in *Drp1*$^{-/-}$ mouse hippocampi did not display a significant change between CT4 and CT16 compared to wild-type controls. Therefore, both *in vivo* and *in vitro*, circadian activation of DRP1 plays a central role in coupling circadian and mitochondrial metabolic cycles.

Overall, these data demonstrate that mitochondrial dynamics are essential for circadian regulation of oxidative metabolism even in non-dividing cells: analysis of DRP1 regulation revealed a circadian Ser637 phosphorylation pattern, and pharmacological or genetic interference with DRP1 activity abolishes circadian ATP production. An important consequence of DRP1 loss is the impairment of mitochondrial architecture and distribution. In brain, this results in impaired synaptic transmission (Oettinghaus et al., 2016, Shields et al., 2015, Verstreken et al.,

2005). Furthermore, DRP1 depletion also affects embryonic and brain development including synapse formation, as well as the survival of post-mitotic neurons (Ishihara et al., 2009, Kageyama et al., 2012). Thus, it cannot be excluded that loss of circadian ATP production could partly also be due to other neuronal dysfunctions besides mitochondrial impairment related to DRP1 loss.

Mitochondrial network retrogradely signals to the molecular core clock.

A known key aspect of circadian oxidative respiration is its ability to feed back to the circadian clock mechanism itself: NAD^+ is a cofactor of the nuclear deacetylase SIRT1, which directly affects circadian clock function (Asher et al., 2008, Nakahata et al., 2008); in addition, purine nucleotide levels modulate AMPK activity to regulate phosphorylation of CRY clock proteins (Lamia et al., 2009, Um et al., 2011). If the morphology-driven circadian control mechanism that we uncovered indeed affected circadian mitochondrial function and ATP levels, one would predict that it should also signal back to modulate circadian function similarly to these other mechanisms. To test this prediction, we lentivirally infected fibroblast cells with a circadian reporter construct (*Bmal1* promoter-driven expression of firefly luciferase) (Brown et al., 2005). As reported previously in other model systems, inhibition of nutrient sensors AMPK, SIRT1, and SIRT3 significantly increased period length (**Fig. 4D, S4E**). Similarly, disruption of mitochondrial division (P110) or calcineurin inhibition (FK506) significantly increased period length (**Fig. 4E, S4F**). These findings are consistent with the idea that DRP1-mediated mitochondrial ATP oscillations may also signal in retrograde fashion to the clock. To confirm this hypothesis, we further analyzed gene expression of the core clock activator *Bmal1* and repressors *Per1* and *Per2* in serum-shocked *Drp1*$^{-/-}$ MEFs (**Fig. 4F, S4D**). Circadian variation in the gene expression of clock activator *Bmal1* and repressors *Per1* and *Per2* was suppressed, confirming that disruption of circadian mitochondrial dynamics leads to an impaired core circadian clock.

Conclusion and Limitations of study

In summary, consistent with the growing body of evidence integrating cellular metabolism with circadian clocks (Ribas-Latre and Eckel-Mahan, 2016), our findings establish a molecular link between circadian control of mitochondrial morphology and oxidative metabolism. It suggests that the global circadian regulation of DRP1-dependent mitochondrial architecture plays a key role in controlling circadian metabolism. Mitochondrial morphology has been demonstrated previously to regulate nearly every aspect of mitochondrial function: mitochondrial fusion to form more extensive tubular networks results in global upregulation of oxidative respiration and all other functions, while fission of mitochondria into smaller fragments achieves the opposite (Westermann, 2010). Such regulation at the level of morphology has been extensively characterized within the context of the cell cycle, where different steps of the cell division process have disparate energy needs (Martinez-Diez et al., 2006, Mishra and Chan, 2014). Here we show that similar morphological control is a crucial node in circadian control of metabolism. Our study focused upon circadian control of the mitochondrial fission protein DRP1. Mitochondrial dynamics are characterized by repeated cycles of fusion and fission, so it is possible that circadian control of fusion, for instance via mitofusins MFN1/2, could also play a physiological role. Moreover, although we demonstrate that circadian control of mitochondrial dynamics is essential for circadian bioenergetics in a number of rodent tissues and cellular models, the exact upstream mechanism of circadian DRP1 phosphorylation remains to be elucidated. The importance of circadian regulation of oxidative phosphorylation is highlighted by the multiple modes of regulation that have been established: via sirtuins and mitochondrial protein acetylation (Peek et al., 2013), via AMPK (Hardie et al., 2012), and here via DRP1 and mitochondrial dynamics. However, connections among these mechanisms remain to be clarified. As here we suggest that mitochondrial dynamics serve as effectors or necessary adjuncts of other circadian signaling to mitochondria, very recent findings in this journal suggest

that they also serve as effectors of diet-mediated longevity (Weir et al., 2017). In reverse, attenuation of mitochondrial dynamics accelerates cardiac senescence (Song et al., 2017). Thus, our findings could have multiple implications in the context of metabolic homeostasis, both with respect to human health and disease, and with respect to impairment in circadian clock and/ or mitochondrial function. Perturbations in the clock might even be a key initiating factor for diseases linked to compromised mitochondrial function, including neurodegenerative disorders such as Alzheimer's disease.

Acknowledgements

This work was supported by Swiss National Science Foundation (#31000_122572 to SAB, SF and AE and #31003A_149728 to AE), Novartis Foundation for Biomedical Research Basel, Synapsis Foundation and the Fonds der Freiwilligen Akademischen Gesellschaft Basel (all to AE). Further support of RD and SAB came from the Swiss National Science Foundation, the University Hospital of Zürich clinical priority program "Sleep and Health", the Fyodor Lynen Foundation, and the Swiss Cancer Society. We thank Ginette Baysang and Fides Meier for technical assistance.

Author Contributions

Conceptualization, SAB and AE; Methodology, SF, SAB, and AE; Investigation, KS, AG, RD, BO, LMR and MW; Writing –Original Draft, KS, AG, SF, SAB and AE; Writing –Review & Editing, KS, AG, SF, SAB and AE; Funding Acquisition, SAB, and AE; Resources, JAR and UA (*mPer1/mPer2*$^{+/+}$ and *mPer1/mPer2*$^{-/-}$ mice), SAB (human glioma A172 cells, human U2OS cells, *mPer1/mPer2*$^{+/+}$ and *mPer1/mPer2*$^{-/-}$ MEFs), NI and KM (*Drp1*$^{flx/flx\ CreERT2}$ mice and *Drp1*$^{lox/lox}$ and *Drp1* $^{-/-}$ MEFs).

Declaration of Interests

The authors declare no competing interests.

References

Adamovich, Y., Rousso-Noori, L., Zwighaft, Z., Neufeld-Cohen, A., Golik, M., Kraut-Cohen, J., Wang, M., Han, X., and Asher, G. (2014). Circadian clocks and feeding time regulate the oscillations and levels of hepatic triglycerides. Cell Metab, 19**,** 319-30.

Ang, J. E., Revell, V., Mann, A., Mantele, S., Otway, D. T., Johnston, J. D., Thumser, A. E., Skene, D. J., and Raynaud, F. (2012). Identification of human plasma metabolites exhibiting time-of-day variation using an untargeted liquid chromatography-mass spectrometry metabolomic approach. Chronobiol Int, 29**,** 868-81.

Asher, G., Gatfield, D., Stratmann, M., Reinke, H., Dibner, C., Kreppel, F., Mostoslavsky, R., Alt, F. W., and Schibler, U. (2008). SIRT1 regulates circadian clock gene expression through PER2 deacetylation. Cell, 134**,** 317-28.

Asher, G., and Schibler, U. (2011). Crosstalk between components of circadian and metabolic cycles in mammals. Cell Metab, 13**,** 125-37.

Balsalobre, A., Damiola, F., and Schibler, U. (1998). A serum shock induces circadian gene expression in mammalian tissue culture cells. Cell, 93**,** 929-37.

Bass, J. (2012). Circadian topology of metabolism. Nature, 491**,** 348-56.

Bordt, E. A., Clerc, P., Roelofs, B. A., Saladino, A. J., Tretter, L., Adam-Vizi, V., Cherok, E., Khalil, A., Yadava, N., Ge, S. X., et al. (2017). The Putative Drp1 Inhibitor mdivi-1 Is a Reversible Mitochondrial Complex I Inhibitor that Modulates Reactive Oxygen Species. Dev Cell, 40**,** 583-594 e6.

Brown, S. A., Fleury-Olela, F., Nagoshi, E., Hauser, C., Juge, C., Meier, C. A., Chicheportiche, R., Dayer, J. M., Albrecht, U., and Schibler, U. (2005). The period length of fibroblast circadian gene expression varies widely among human individuals. PLoS Biol, 3**,** e338.

Brunner, M., and Schafmeier, T. (2006). Transcriptional and post-transcriptional regulation of the circadian clock of cyanobacteria and Neurospora. Genes Dev, 20**,** 1061-74.

Cereghetti, G. M., Stangherlin, A., Martins De Brito, O., Chang, C. R., Blackstone, C., Bernardi, P., and Scorrano, L. (2008). Dephosphorylation by calcineurin regulates translocation of Drp1 to mitochondria. Proc Natl Acad Sci U S A, 105**,** 15803-8.

Chang, C. R., and Blackstone, C. (2007). Cyclic AMP-dependent protein kinase phosphorylation of Drp1 regulates its GTPase activity and mitochondrial morphology. J Biol Chem, 282**,** 21583-7.

Cribbs, J. T., and Strack, S. (2007). Reversible phosphorylation of Drp1 by cyclic AMP-dependent protein kinase and calcineurin regulates mitochondrial fission and cell death. EMBO Rep, 8**,** 939-44.

Dallmann, R., Viola, A. U., Tarokh, L., Cajochen, C., and Brown, S. A. (2012). The human circadian metabolome. Proc Natl Acad Sci U S A, 109**,** 2625-9.

Davies, S. K., Ang, J. E., Revell, V. L., Holmes, B., Mann, A., Robertson, F. P., Cui, N., Middleton, B., Ackermann, K., Kayser, M., et al. (2014). Effect of sleep deprivation on the human metabolome. Proc Natl Acad Sci U S A, 111**,** 10761-6.

Eckel-Mahan, K., and Sassone-Corsi, P. (2013). Metabolism and the circadian clock converge. Physiol Rev, 93**,** 107-35.

Eckel-Mahan, K. L., Patel, V. R., Mohney, R. P., Vignola, K. S., Baldi, P., and Sassone-Corsi, P. (2012). Coordination of the transcriptome and metabolome by the circadian clock. Proc Natl Acad Sci U S A, 109**,** 5541-6.

Feng, D., Liu, T., Sun, Z., Bugge, A., Mullican, S. E., Alenghat, T., Liu, X. S., and Lazar, M. A. (2011). A circadian rhythm orchestrated by histone deacetylase 3 controls hepatic lipid metabolism. Science, 331**,** 1315-9.

Gachon, F., Nagoshi, E., Brown, S. A., Ripperger, J., and Schibler, U. (2004). The mammalian circadian timing system: from gene expression to physiology. Chromosoma, 113**,** 103-12.

Gaspar, L., and Brown, S. A. (2015). Measuring circadian clock function in human cells. Methods Enzymol, 552**,** 231-56.

Gertz, M., Fischer, F., Nguyen, G. T., Lakshminarasimhan, M., Schutkowski, M., Weyand, M., and Steegborn, C. (2013). Ex-527 inhibits Sirtuins by exploiting their unique NAD+-dependent deacetylation mechanism. Proc Natl Acad Sci U S A, 110**,** E2772-81.

Gomes, L. C., Di Benedetto, G., and Scorrano, L. (2011). During autophagy mitochondria elongate, are spared from degradation and sustain cell viability. Nat Cell Biol, 13**,** 589-98.

Hanson, G. T., Aggeler, R., Oglesbee, D., Cannon, M., Capaldi, R. A., Tsien, R. Y., and Remington, S. J. (2004). Investigating mitochondrial redox potential with redox-sensitive green fluorescent protein indicators. J Biol Chem, 279**,** 13044-53.

Hardie, D. G., Ross, F. A., and Hawley, S. A. (2012). AMPK: a nutrient and energy sensor that maintains energy homeostasis. Nat Rev Mol Cell Biol, 13**,** 251-62.

Huang, C. C., Ko, M. L., Vernikovskaya, D. I., and Ko, G. Y. (2012). Calcineurin serves in the circadian output pathway to regulate the daily rhythm of L-type voltage-gated calcium channels in the retina. J Cell Biochem, 113**,** 911-22.

Hughes, M. E., Hogenesch, J. B., and Kornacker, K. (2010). JTK_CYCLE: an efficient nonparametric algorithm for detecting rhythmic components in genome-scale data sets. J Biol Rhythms, 25**,** 372-80.

Invernizzi, F., D'amato, I., Jensen, P. B., Ravaglia, S., Zeviani, M., and Tiranti, V. (2012). Microscale oxygraphy reveals OXPHOS impairment in MRC mutant cells. Mitochondrion, 12**,** 328-35.

Ishihara, N., Nomura, M., Jofuku, A., Kato, H., Suzuki, S. O., Masuda, K., Otera, H., Nakanishi, Y., Nonaka, I., Goto, Y., et al. (2009). Mitochondrial fission factor Drp1 is essential for embryonic development and synapse formation in mice. Nat Cell Biol, 11**,** 958-66.

Isobe, Y., Hida, H., and Nishino, H. (2011). Circadian rhythm of metabolic oscillation in suprachiasmatic nucleus depends on the mitochondrial oxidation state, reflected by cytochrome C oxidase and lactate dehydrogenase. J Neurosci Res, 89**,** 929-35.

Jacobi, D., Liu, S., Burkewitz, K., Kory, N., Knudsen, N. H., Alexander, R. K., Unluturk, U., Li, X., Kong, X., Hyde, A. L., et al. (2015). Hepatic Bmal1 Regulates Rhythmic Mitochondrial Dynamics and Promotes Metabolic Fitness. Cell Metab, 22**,** 709-20.

Kageyama, Y., Zhang, Z., Roda, R., Fukaya, M., Wakabayashi, J., Wakabayashi, N., Kensler, T. W., Reddy, P. H., Iijima, M., and Sesaki, H. (2012). Mitochondrial division ensures the survival of postmitotic neurons by suppressing oxidative damage. J Cell Biol, 197**,** 535-51.

Kanfer, G., and Kornmann, B. (2016). Dynamics of the mitochondrial network during mitosis. Biochem Soc Trans, 44**,** 510-6.

Kasukawa, T., Sugimoto, M., Hida, A., Minami, Y., Mori, M., Honma, S., Honma, K., Mishima, K., Soga, T., and Ueda, H. R. (2012). Human blood metabolite timetable indicates internal body time. Proc Natl Acad Sci U S A, 109**,** 15036-41.

Koopman, W. J., Verkaart, S., Visch, H. J., Van Der Westhuizen, F. H., Murphy, M. P., Van Den Heuvel, L. W., Smeitink, J. A., and Willems, P. H. (2005). Inhibition of complex I of the electron transport chain causes O2-. -mediated mitochondrial outgrowth. Am J Physiol Cell Physiol, 288**,** C1440-50.

Lamia, K. A., Papp, S. J., Yu, R. T., Barish, G. D., Uhlenhaut, N. H., Jonker, J. W., Downes, M., and Evans, R. M. (2011). Cryptochromes mediate rhythmic repression of the glucocorticoid receptor. Nature, 480**,** 552-6.

Lamia, K. A., Sachdeva, U. M., Ditacchio, L., Williams, E. C., Alvarez, J. G., Egan, D. F., Vasquez, D. S., Juguilon, H., Panda, S., Shaw, R. J., et al. (2009). AMPK regulates the circadian clock by cryptochrome phosphorylation and degradation. Science, 326**,** 437-40.

Lawton, K. A., Berger, A., Mitchell, M., Milgram, K. E., Evans, A. M., Guo, L., Hanson, R. W., Kalhan, S. C., Ryals, J. A., and Milburn, M. V. (2008). Analysis of the adult human plasma metabolome. Pharmacogenomics, 9**,** 383-97.

Lopez-Mejia, I. C., and Fajas, L. (2015). Cell cycle regulation of mitochondrial function. Curr Opin Cell Biol, 33**,** 19-25.

Manella, G., and Asher, G. (2016). The Circadian Nature of Mitochondrial Biology. Front Endocrinol (Lausanne), 7**,** 162.

Marcussen, M., and Larsen, P. J. (1996). Cell cycle-dependent regulation of cellular ATP concentration, and depolymerization of the interphase microtubular network induced by elevated cellular ATP concentration in whole fibroblasts. Cell Motil Cytoskeleton, 35**,** 94-9.

Martinez-Diez, M., Santamaria, G., Ortega, A. D., and Cuezva, J. M. (2006). Biogenesis and dynamics of mitochondria during the cell cycle: significance of 3'UTRs. PLoS One, 1**,** e107.

Masri, S., Patel, V. R., Eckel-Mahan, K. L., Peleg, S., Forne, I., Ladurner, A. G., Baldi, P., Imhof, A., and Sassone-Corsi, P. (2013). Circadian acetylome reveals regulation of mitochondrial metabolic pathways. Proc Natl Acad Sci U S A, 110**,** 3339-44.

Matsuo, T., Yamaguchi, S., Mitsui, S., Emi, A., Shimoda, F., and Okamura, H. (2003). Control mechanism of the circadian clock for timing of cell division in vivo. Science, 302**,** 255-9.

Mcginnis, G. R., and Young, M. E. (2016). Circadian regulation of metabolic homeostasis: causes and consequences. Nat Sci Sleep, 8**,** 163-80.

Minami, Y., Kasukawa, T., Kakazu, Y., Iigo, M., Sugimoto, M., Ikeda, S., Yasui, A., Van Der Horst, G. T., Soga, T., and Ueda, H. R. (2009). Measurement of internal body time by blood metabolomics. Proc Natl Acad Sci U S A, 106**,** 9890-5.

Mishra, P., and Chan, D. C. (2014). Mitochondrial dynamics and inheritance during cell division, development and disease. Nat Rev Mol Cell Biol, 15**,** 634-46.

Nagoshi, E., Saini, C., Bauer, C., Laroche, T., Naef, F., and Schibler, U. (2004). Circadian gene expression in individual fibroblasts: cell-autonomous and self-sustained oscillators pass time to daughter cells. Cell, 119**,** 693-705.

Nakahata, Y., Kaluzova, M., Grimaldi, B., Sahar, S., Hirayama, J., Chen, D., Guarente, L. P., and Sassone-Corsi, P. (2008). The NAD+-dependent deacetylase SIRT1 modulates CLOCK-mediated chromatin remodeling and circadian control. Cell, 134**,** 329-40.

Nakahata, Y., Sahar, S., Astarita, G., Kaluzova, M., and Sassone-Corsi, P. (2009). Circadian control of the NAD+ salvage pathway by CLOCK-SIRT1. Science, 324**,** 654-7.

Neufeld-Cohen, A., Robles, M. S., Aviram, R., Manella, G., Adamovich, Y., Ladeuix, B., Nir, D., Rousso-Noori, L., Kuperman, Y., Golik, M., et al. (2016). Circadian control of oscillations in mitochondrial rate-limiting enzymes and nutrient utilization by PERIOD proteins. Proc Natl Acad Sci U S A, 113**,** E1673-82.

O'neill, J. S., Maywood, E. S., Chesham, J. E., Takahashi, J. S., and Hastings, M. H. (2008). cAMP-dependent signaling as a core component of the mammalian circadian pacemaker. Science, 320**,** 949-53.

Oettinghaus, B., Schulz, J. M., Restelli, L. M., Licci, M., Savoia, C., Schmidt, A., Schmitt, K., Grimm, A., More, L., Hench, J., et al. (2016). Synaptic dysfunction, memory deficits and hippocampal atrophy due to ablation of mitochondrial fission in adult forebrain neurons. Cell Death Differ, 23**,** 18-28.

Oosterman, J. E., and Belsham, D. D. (2016). Glucose Alters Per2 Rhythmicity Independent of AMPK, Whereas AMPK Inhibitor Compound C Causes Profound Repression of Clock Genes and AgRP in mHypoE-37 Hypothalamic Neurons. PLoS One, 11**,** e0146969.

Otera, H., Ishihara, N., and Mihara, K. (2013). New insights into the function and regulation of mitochondrial fission. Biochim Biophys Acta, 1833**,** 1256-68.

Outeiro, T. F., Kontopoulos, E., Altmann, S. M., Kufareva, I., Strathearn, K. E., Amore, A. M., Volk, C. B., Maxwell, M. M., Rochet, J. C., Mclean, P. J., et al. (2007). Sirtuin 2 inhibitors rescue alpha-synuclein-mediated toxicity in models of Parkinson's disease. Science, 317**,** 516-9.

Pagani, L., Schmitt, K., Meier, F., Izakovic, J., Roemer, K., Viola, A., Cajochen, C., Wirz-Justice, A., Brown, S. A., and Eckert, A. (2011). Serum factors in older individuals change cellular clock properties. Proc Natl Acad Sci U S A, 108**,** 7218-23.

Panda, S., Antoch, M. P., Miller, B. H., Su, A. I., Schook, A. B., Straume, M., Schultz, P. G., Kay, S. A., Takahashi, J. S., and Hogenesch, J. B. (2002). Coordinated transcription of key pathways in the mouse by the circadian clock. Cell, 109**,** 307-20.

Peek, C. B., Affinati, A. H., Ramsey, K. M., Kuo, H. Y., Yu, W., Sena, L. A., Ilkayeva, O., Marcheva, B., Kobayashi, Y., Omura, C., et al. (2013). Circadian clock NAD+ cycle drives mitochondrial oxidative metabolism in mice. Science, 342**,** 1243417.

Qi, X., Qvit, N., Su, Y. C., and Mochly-Rosen, D. (2013). A novel Drp1 inhibitor diminishes aberrant mitochondrial fission and neurotoxicity. J Cell Sci, 126**,** 789-802.

Ramsey, K. M., Yoshino, J., Brace, C. S., Abrassart, D., Kobayashi, Y., Marcheva, B., Hong, H. K., Chong, J. L., Buhr, E. D., Lee, C., et al. (2009). Circadian clock feedback cycle through NAMPT-mediated NAD+ biosynthesis. Science, 324**,** 651-4.

Ribas-Latre, A., and Eckel-Mahan, K. (2016). Interdependence of nutrient metabolism and the circadian clock system: Importance for metabolic health. Mol Metab, 5**,** 133-52.

Rosato, E., Tauber, E., and Kyriacou, C. P. (2006). Molecular genetics of the fruit-fly circadian clock. Eur J Hum Genet, 14**,** 729-38.

Schmutz, I., Ripperger, J. A., Baeriswyl-Aebischer, S., and Albrecht, U. (2010). The mammalian clock component PERIOD2 coordinates circadian output by interaction with nuclear receptors. Genes Dev, 24**,** 345-57.

Shields, L. Y., Kim, H., Zhu, L., Haddad, D., Berthet, A., Pathak, D., Lam, M., Ponnusamy, R., Diaz-Ramirez, L. G., Gill, T. M., et al. (2015). Dynamin-related protein 1 is required for normal mitochondrial bioenergetic and synaptic function in CA1 hippocampal neurons. Cell Death Dis, 6**,** e1725.

Song, M., Franco, A., Fleischer, J. A., Zhang, L., and Dorn, G. W., 2nd (2017). Abrogating Mitochondrial Dynamics in Mouse Hearts Accelerates Mitochondrial Senescence. Cell Metab, 26**,** 872-883 e5.

Um, J. H., Pendergast, J. S., Springer, D. A., Foretz, M., Viollet, B., Brown, A., Kim, M. K., Yamazaki, S., and Chung, J. H. (2011). AMPK regulates circadian rhythms in a tissue- and isoform-specific manner. PLoS One, 6**,** e18450.

Verstreken, P., Ly, C. V., Venken, K. J., Koh, T. W., Zhou, Y., and Bellen, H. J. (2005). Synaptic mitochondria are critical for mobilization of reserve pool vesicles at Drosophila neuromuscular junctions. Neuron, 47**,** 365-78.

Vollmers, C., Gill, S., Ditacchio, L., Pulivarthy, S. R., Le, H. D., and Panda, S. (2009). Time of feeding and the intrinsic circadian clock drive rhythms in hepatic gene expression. Proc Natl Acad Sci U S A, 106**,** 21453-8.

Wai, T., and Langer, T. (2016). Mitochondrial Dynamics and Metabolic Regulation. Trends Endocrinol Metab, 27**,** 105-17.

Wang, J. X., Jiao, J. Q., Li, Q., Long, B., Wang, K., Liu, J. P., Li, Y. R., and Li, P. F. (2011). miR-499 regulates mitochondrial dynamics by targeting calcineurin and dynamin-related protein-1. Nat Med, 17**,** 71-8.

Weir, H. J., Yao, P., Huynh, F. K., Escoubas, C. C., Goncalves, R. L., Burkewitz, K., Laboy, R., Hirschey, M. D., and Mair, W. B. (2017). Dietary Restriction and AMPK Increase Lifespan via Mitochondrial Network and Peroxisome Remodeling. Cell Metab, 26**,** 884-896 e5.

Westermann, B. (2010). Mitochondrial fusion and fission in cell life and death. Nat Rev Mol Cell Biol, 11**,** 872-84.

Zhang, Y., Fang, B., Emmett, M. J., Damle, M., Sun, Z., Feng, D., Armour, S. M., Remsberg, J. R., Jager, J., Soccio, R. E., et al. (2015). GENE REGULATION. Discrete functions of nuclear receptor Rev-erbalpha couple metabolism to the clock. Science, 348**,** 1488-92.

Zheng, B., Albrecht, U., Kaasik, K., Sage, M., Lu, W., Vaishnav, S., Li, Q., Sun, Z. S., Eichele, G., Bradley, A., et al. (2001). Nonredundant roles of the mPer1 and mPer2 genes in the mammalian circadian clock. Cell, 105**,** 683-94.

Main figure titles and legends

Figure 1: OxPhos-dependent ATP variations are driven by the circadian clock.

(**A**) Percentage of non-circadian and circadian metabolites based on JTK_CYCLE analysis (n=2 per time point). Metabolites were considered circadian at a p-value cutoff of 0.05.

(**B, C**) Compound class (**B**) and time-of-day distribution of peak phases (**C**) of rhythmic metabolites.

(**D**) Relative total ATP level measured in serum-shocked *Per1/2*$^{-/-}$ MEFs compared to WT MEFs (n=6 per time point, JTK_Cycle, P_{WT}=0.000179, P_{KO}=0.39). Right panel displays relative total ATP level measured in serum-shocked *Per1/2*$^{-/-}$ MEFs compared to WT MEFs at 16 hours post-shock (peak of ATP content) and at 28 hours (trough of ATP content).

(**E**) Relative total ATP levels from serum-shocked human skin fibroblasts treated with 2 - deoxy-D-glucose (2DG, 4.5 g/L) or oligomycin (OLIGO, 2 μM) compared to non-treated cells (CTRL) measured at the indicated time points (n=6 per time point, JTK_Cycle, P_{CTRL}=1.78*10^{-15}, P_{2DG}=9.78*10^{-06}, P_{Oligo}=0.461). Right panel displays relative total ATP level at 16 hours post-shock (peak of ATP content) and at 28 hours (trough of ATP content) in control and treated conditions.

Data are represented as average ± SEM. **P<0.01, ***P<0.001 for Student's two-tailed t test comparing single time points between WT and mutant (**D**) or CTRL and treated cells (**E**).

(**F**) Oxygen Consumption Rate (OCR) was evaluated in serum-shocked fibroblasts treated sequentially with oligomycin (Oligo, 2 μM), a mitochondrial ATP synthesis inhibitor; FCCP [carbonyl cyanide p (trifluoromethoxy) phenylhydrazone] (0.7 μM), an uncoupling agent allowing measurement of maximal flux; rotenone (ROT, 2 μM), a complex I inhibitor; and antimycin A (AA, 4 μM), a cytochrome C reductase inhibitor that blocks OxPhos, at 16 and 28 hours post-shock, respectively.

(**G**) Bioenergetic profile of synchronized fibroblasts at 16 and 28 hours post-shock, respectively. Basal respiration, ATP turnover and maximal respiration are determined after normalization to OCR allocated to non-mitochondrial respiration measured after antimycin A/ rotenone injection.

(**H**) Cellular bioenergetic profile (OCR versus ECAR) evaluated at 16 and 28 hours post-shock, respectively, in human skin fibroblasts. Black arrow corresponds to the metabolic switch from a metabolically active (16 hours) to a resting state (28 hours).

Data are represented as average ± SEM (n= 11 replicates per time point, three independent experiments) (**F-H**). **P<0.01, ***P<0.001 for Student's two-tailed t test comparing time points.

See also Figures S1, S2 and Table S1.

Figure 2: Dynamic mitochondrial architecture is controlled by the circadian clock.

(**A, B**) Mitochondrial network morphology assessed in serum-shocked human skin fibroblasts at 16 (**A**) and 28 (**B**) hours, corresponding to a tubular network and a fragmented network, respectively. For each representative image (**A**) (**ii**) and (**B**) (**ii**), a zoom-in image is shown (400%). (**A**) (**i**) and (**B**) (**i**): scale bar = 100 µm. (**A**) (**ii**) and (**B**) (**ii**): scale bar = 25 µm.

(**C, D**) Mitochondrial network morphology assessed in hippocampal CA1 region from non-fasted wild-type mice kept (**C**) in darkness condition at CT0 (**i**) and CT12 (**ii**) and from *mPer1/mPer2* double mutant mice (**D**) in darkness condition at CT0 (**i**) and CT12 (**ii**).

(**E**) Quantification of mitochondrial interconnectivity in clock-synchronized fibroblasts during 40 hours. On average 3000-10,000 mitochondrial organelles were analyzed per time point (n = 25-30 images per time point, JTK_Cycle, P=0.000719); images for additional time points in Fig **S2**.

(**F**) Quantification of mitochondrial interconnectivity from non-fasted wild-type mice kept ad from *mPer1/mPer2* double mutant mice in darkness condition at CT0 and CT12. On average 3000-10,000 mitochondrial organelles were analyzed per time point (n=6 sections per condition). Data are represented as average ± SEM (**E-F**). ***P<0.001 for Student's two-tailed t test comparing time points (e.g. 16h versus 28h) (**E**) or comparing single time points between WT and mutant (**F**).

See also Figures S2 and S3.

Figure 3: DRP1 phosphorylation is under clock control.

(**A**) Left panel, representative phosphorylation of DRP1 on serine 637 (P-DRP1) and total DRP1 evaluated at the indicated time points in serum-shocked human skin fibroblasts. Right panel, quantification of relative DRP1 phosphorylation normalized to calibration sample (n=6 per time point, JTK_Cycle, $P_{P\text{-}DRP1}$=0.000628, P_{DRP1}=0.815).

(**B**) Left panel, representative phosphorylation of DRP1 on serine 637 (P-DRP1) and total DRP1 evaluated at the indicated time points in brain homogenate of non-fasted wild-type mice kept in constant darkness (represented by the black bar). Right panel, quantification of relative DRP1 phosphorylation normalized to calibration sample measured in brain homogenate (n=4 per time point, JTK_Cycle, $P_{P\text{-}DRP1}$=0.000265, P_{DRP1}=0.549).

(**C**) Representative phosphorylation of DRP1 on serine 637 (P-DRP1) and total DRP1 levels evaluated at the indicated time points in brain homogenate of non-fasted *mPer1/mPer2* double mutant mice kept in constant darkness.

(**D-G**) Representative phosphorylation of DRP1 on serine 637 (P-DRP1) and total DRP1 evaluated at the indicated time points in serum-shocked human skin fibroblasts in presence of inhibitors of calcineurin (FK506, 1 μM) (**D**), AMPK (compound C, 1 μM) (**E**), sirtuin 1 (Ex527. 1 μM) (**F**) or sirtuin 3 (AGK7, 1 μM) (**G**).

Figure 4: Mitochondrial metabolism is dependent upon DRP1-related clock regulation and feeds back to the molecular core clock.

(**A**) Left panel, relative total ATP levels from serum-shocked human skin fibroblasts treated with P110 (1 μM) compared to non-treated cells (CTRL) measured at the indicated time points (n=6 per time point, JTK_Cycle, $P_{CTRL}=5.36*10^{-20}$, $P_{P110}=0.7592$). Right panel, relative total ATP level at 16 hours post-shock (peak of ATP content) and at 28 hours (trough of ATP content) in control and treated conditions.

(**B**) Left panel, relative total ATP levels from *Drp1* $^{-/-}$ MEFs compared to *Drp1*$^{lox/lox}$ MEFs measured at the indicated time points (n=6 per time point, JTK_Cycle, $P_{Drp1}{}^{lox/lox} = 6.83*10^{-12}$, $P_{Drp1}{}^{-/-} = 0.2608$). Right panel, relative total ATP level at 16 hours post-shock (peak of ATP content) and at 28 hours (trough of ATP content) in *Drp1*$^{lox/lox}$ MEFs and *Drp1* $^{-/-}$ MEFs

(**C**) Total ATP levels from hippocampus of non-fasted *Drp1* $^{-/-}$ mice compared to *Drp1*$^{lox/lox}$ mice kept in constant darkness measured at CT4 (peak of ATP content) and at CT16 (trough of ATP content) (n=4 per time point).

Data are represented as average ± SEM (**A-C**). ***P<0.001 for Student's two-tailed t test comparing single time points between CTRL and treated cells (**A**) or WT and mutant (**B, C**).

(**D**) Circadian period length determined in dexamethasone - synchronized human skin fibroblasts transfected with Bmal1::luciferase reporter in presence of an AMPK inhibitor (compound C, 1 μM), a SIRT1 inhibitor (Ex527, 1 μM) and a SIRT3 inhibitor (AGK7, 1 μM) (C) compared to control (CTRL).

(**E**) Circadian period length determined in dexamethasone - synchronized human skin fibroblasts transfected with Bmal1::luciferase reporter in presence of complex I inhibitor Mdivi-1 (50 μM) or DRP1 inhibitor P110 (1 μM), and calcineurin inhibitor (FK506, 1 μM) compared to control (CTRL).

(**F**) Relative mRNA expression of Bmal1, Per1 and Per2 evaluated from in *Drp1* $^{-/-}$ MEFs compared to *Drp1*$^{lox/lox}$ MEFs at 12 hours and 24 hours (n=6 per time point).

Bars represent the mean of three independent measurements ± SEM (**D- F**). ***P < 0.001 for Student's two-tailed t-test comparing CTRL and treated cells (**D, E) or** comparing single time points between WT and mutant (**F**).

See also Figure S4.

STAR Methods

Contact for reagent and resource sharing

Further information and requests for resources and reagents should be directed to and will be fulfilled by the Lead Contact, Anne Eckert *(*anne.eckert@upkbs.ch*)*.

Experimental model and subject details

Mice

Drp1$^{flx/flx\ CreERT2}$ mice were obtained by crossing *Drp1*$^{flx/flx}$ mice with mice expressing an inducible Cre recombinase transgene under the control of the CamKIIα promoter (Cre^{+}), which is active in the hippocampus and the cortex of adult mice (from the European Mouse Mutant Archive EMMA strain 02125) (Ishihara et al., 2009). At 8 weeks of age mice were injected intraperitoneally with 1 mg tamoxifen twice daily for five consecutive days to induce recombination of the Drp1 locus (Oettinghaus et al., 2016). *mPer1/mPer2* double mutant mice were generated as described previously (Zheng et al., 2001).

Male C57BL/6, *Drp1*$^{flx/flx\ CreERT2}$ and *mPer1*/*mPer2* double-mutant mice (10-12 weeks old) were housed at 24°C for one week on a 12:12 light-dark cycle prior to placement in constant darkness 5 days before the beginning of the experiment with free access to ordinary food (normal chow) and water. Circadian time 0 (CT0) is the start of subjective daytime and CT12 is the start of subjective night-time, under constant dark conditions, over 24 hours. Experiments were performed in compliance with protocols approved by the local Basel Committee for Animal Care and Animal Use.

Cell culture

Human osteosarcoma U2OS cells (derived from a 15-years-old female donor) and human skin fibroblasts (derived from a 31-years-old male donor) infected with lentiviral circadian reporter mice Bmal1::luciferase were cultured at 37 C in a humidified incubator chamber under an atmosphere of 7.5% CO_2 in complete Dulbecco's modified Eagle's medium (DMEMc, including

1% penicillin/streptomycin, 1% glutamax) supplemented with 20% fetal bovine serum (FBS) as described previously (Brown et al., 2005).

Human glioma A172 cells were transfected with plasmid DNA of a mitochondrial targeted GFP (pEGFP-N1-mt-ro2GFP) (Hanson et al., 2004) using the Lipofectamine 2000 reagent. After transfection, cells were selected in DMEMc supplemented with 10% FBS and 300 μg/ml of the antibiotic Geneticin for two months at 37 C in a humidified incubator chamber under an atmosphere of 7.5% CO_2. Glioma cells were also infected with lentiviral circadian reporter mice *Bmal1*::luciferase and the circadian period length was then determined to ensure that cells have normal circadian rhythms (protocol details in the ***Circadian period length determination*** section; data not shown: mean period length of 3 independents experiments 25.44 +/- SEM 0.4865 hours).

Drp1$^{lox/lox}$ MEFs were prepared from E13.5 *Drp1*$^{lox/lox}$ embryos and cultured as previously described (Ishihara et al., 2009). *Drp1*$^{-/-}$ MEFs were subsequently generated by expression of Cre recombinase. The MEFs were maintained in DMEMc supplemented with 10% FBS and 1x non-essential amino acids cultured at 37 C in a humidified incubator chamber under an atmosphere of 7.5% CO_2.

MEFs lacking *mPer1* and *mPer2* isolated from double knockout mice were generated from E12 embryos as previously described (Nagoshi et al., 2004, Zheng et al., 2001) and cultured in DMEMc supplemented with 10% FBS cultured at 37 C in a humidified incubator chamber under an atmosphere of 7.5% CO_2.

Method details

Brain homogenate preparation

Brains were dissected on ice and washed in ice-cold buffer (210 mM mannitol, 70 mM sucrose, 10 mM Hepes, 1 mM EDTA, 0.45% BSA, 0.5 mM DTT, and Complete Protease Inhibitor mixture tablets). After removing the cerebellum, tissue samples were homogenized in 2 ml of

buffer with a glass homogenizer (10–15 strokes, 400 rpm). After protein concentration determination, all brain homogenate samples were normalized on 5 mg/ml of protein before ATP content measurement and on 1 mg/ml for NAD^+/NADH content determination.

Synchronization of circadian rhythms

For small-molecule and period length determination, cells were synchronized by addition of 100 nM dexamethasone in DMEMc + 20% FBS for 15 mins at 37 °C (Brown et al., 2005). For measurements of nucleotides levels, cell proliferation, reactive oxygen species, oxygen consumption rate and mitochondrial morphology, cells were synchronized by serum shock treatment (50% horse serum supplemented DMEMc) (Balsalobre et al., 1998).

Small-Molecule determination.

After dexamethasone- synchronization of circadian rhythms in U2OS cells, metabolites were measured from duplicate plates by Metabolon (Morrisville, NC), and data was processed as described previously (Dallmann et al., 2012, Lawton et al., 2008). Briefly, raw peak values of each biochemical were re-scaled to have median equal to 1. Because the absolute levels and thus the lower limit of detection were unknown, missing values were replaced by the minimum values observed for any given metabolite. This procedure prevented overestimation of circadian amplitude in less abundant substances, whose true minimum values are unknown.

Nucleotide measurements

Total ATP content from synchronized human skin fibroblasts, *Drp1*$^{lox/lox}$ and *Drp1*$^{-/-}$ MEFs, *Per1/2*$^{+/+}$ *and* *Per1/2*$^{-/-}$ MEFs and mice brain homogenates was determined using bioluminescence assay according to the instruction of the manufacturer. Briefly, the enzyme luciferase, which catalyzes the formation of light from ATP and luciferin was used. The emitted light is linearly related to the ATP concentration and is measured using a luminometer (VictorX5, Perkin Elmer). To define the origin of ATP oscillations, DMEMc without phenol red

+ 2% FBS supplemented with 2-Deoxy-D-glucose (4.5 g/l), a glycolysis inhibitor, and pyruvate (4 mM) or oligomycin (2 μM), an ATP synthase inhibitor, was added on synchronized human skin fibroblasts. To test the possibility that rhythmic ATP is a byproduct of rhythmic cell division, pharmacological disruption of the cell cycle was accomplished with the inhibitor AraC, an anticancer drug that prevents cell division (100 μm). AraC was added to human skin fibroblasts cultures 3 hours after the seeding, directly after the medium exchange following the synchronization and then every 24 hours to assure continued block of cell division. To verify if AraC treatment had an impact on cell cycle and blocked cell proliferation, the BrdU Cell Proliferation Assay was used following the instructions of the manufacturer. To investigate the role of clock- regulated DRP1 in mitochondrial bioenergetics, mitochondrial fission was abolished by selective inhibition of DRP1 using the inhibitor P110 (1 μM) or inhibition of complex I using the inhibitor Mdivi-1 (50 μM).

For measurement of NAD^+ and NADH from synchronized fibroblasts and mice brain homogenates, NAD^+ and NADH were separately extracted using an acid-base extraction (HCL 0.1 mol/l – NAOH 0.1 mol/l). The determination of both NAD^+ and NADH was performed using an enzyme cycling assay based on passing the electron from ethanol trough reduced pyridine nucleotides to MTT (3-(4,5-Dimethylthiazol-2-yl)-2,5-diphenyltetrazolium bromide) in a PES-(phenazine ethosulfate) coupled reaction resulting in a purple formazan product that can be quantitatively measured at a wavelength of 595 nm (VictorX5, Perkin Elmer).

Experiments were performed starting from 12 hours post-synchronization time point and measured at 4 hours intervals for 6 time points.

ROS level

The formation of cytosolic (cROS), mitochondrial (mROS) reactive oxygen species and superoxide anions in synchronized fibroblasts were measured using, the fluorescent probe 2',7'-dichlorofuorescin diacetate (DCF) (10 μM, 15 min), the non-fluorescent dihydrorhodamine-123

(DHR) (10 μM, 15 min) and the Red Mitochondrial Superoxide Indicator (MitoSOX, 5 μM, 30 min), respectively.

Synchronized fibroblasts were loaded for 15 min with 10 μM DCF or 15 min with 10 μM DHR at 37 °C. After washing twice with HBSS, the formation of the reduced fluorescent product dichlorofluorescein was detected using the VictorX5 multilabel reader (PerkinElmer Life Sciences) at 485 nm (excitation)/535 nm (emission). DHR, which is oxidized to cationic rhodamine 123 which localizes in the mitochondria and exhibits green fluorescence, was detected using the VictorX5 multilabel reader at 490 nm (excitation)/590 nm (emission). The levels of superoxide anion radical were also assessed using the Red Mitochondrial Superoxide Indicator (MitoSOX, 5 μM, 30 min). MitoSOX, which is specifically oxidized by mitochondrial superoxide, exhibits a red fluorescence detected at 535 nm (excitation)/595 nm (emission). The intensity of fluorescence was proportional to mROS levels or superoxide anion radicals in mitochondria. Experiments were performed starting from 12 hours post-synchronization time point and measured at 4 hours intervals.

Oxygen Consumption Rate (OCR) measurements

OCR was measured in synchronized fibroblasts as recommended as previously described (Invernizzi et al., 2012). Briefly, human skin fibroblasts were seeded at the density of $3x10^4$ cells/100 μl per well on Seahorse Biosciences 24-well culture plates one day prior to the beginning of assay. After serum shock synchronization, medium was exchanged to 500 μl of assay medium (glucose-free RPMI-1640 medium containing 2% FBS, 2 mM sodium pyruvate, pH ~ 7.4). Prior to measurements the microplates were equilibrated in a CO_2 free incubator at 37 °C for 60 minutes. The drug injections ports of the XF Assay Cartridge were loaded with the assay reagents at 10X in assay medium. 55 μl of oligomycin (10 μM), 62 μl of FCCP (7 μM), 68μl of a mix of antimycin A (40 μM) and rotenone (20 μM) were added to ports A, B and C respectively. Experiments were performed at 16 hours post-shock and 28 hours post-shock.

Mitochondrial morphology

Human skin fibroblast and mitochondrial targeted GFP transfected human glioma A172 cells were cultured on glass coverslips. Mitochondrial staining was performed on serum-shocked fibroblasts with the mitochondrial membrane potential-sensitive dye Mitotracker® Red CMX ROS (75nM, 15 minutes, 579/599, Life technologies). After PFA fixation, the coverslips were mounting using ProLong® Gold antifade reagent.

For immunohistochemistry on brain and liver (hippocampus (CA1 region) and liver sections from C57BL/6 mice and from *mPer1*/*mPer2* double-mutant mice at CT0, onset of subjective day or rest period, and CT12, onset of subjective night or activity period), antibody against the outer mitochondrial membrane porin, Voltage-Dependent Anionic Channel (VDAC, 1:75) was used for determining mitochondrial morphology. A FITC-labeled anti-rabbit IgG (1:160, 490/525) was used as secondary antibody. TO-PRO-3iode (1uM, 642/661) was used as nuclei staining according to the manufacturer's recommendation.

The acquisition of XY-confocal images with maximum intensity projection was performed using an inverted microscope (Leica Microsystems TCS SPE DMI4000) attached to an external light source for enhanced fluorescence imaging (Leica EL6000) with a ×63 oil immersion objective (numerical aperture 1.4; Leica). Given the flat morphology of the fibroblasts (size <3 μm in the axial direction), pinhole settings were chosen in such a way that axially each cell was entirely present within the confocal volume. For morphological analysis, the samples were blindly analyzed. The form factor as measurement of mitochondrial interconnectivity was calculated for each mitochondrial object using NIH ImageJ software (Koopman et al., 2005) . The degree of mitochondrial interconnectivity ($perimeter^2/4*Pi*Area$) is a measure of both length and degree of branching. A degree of interconnectivity of 1 corresponds to a circular, unbranched mitochondrion whereas a higher degree of interconnectivity indicates a longer, more branched mitochondrion.

Protein gel electrophoresis and immunoblotting

Lysates from serum-shocked fibroblast cultures and brain homogenate were prepared and protein expression levels were measured by standard western blot procedure. A calibration sample corresponding to an assembling of all the time points was also measure for normalization. We used primary antibodies to DRP1 (1:500, Cell Signaling), ser637-phosphorylated DRP1 (1:500, Cell Signaling) and VDAC (1:500, Cell Signaling) and horseradish peroxidase-coupled IgG as secondary antibody (1:160, Sigma). Signals were detected by enhanced chemiluminescence using SuperSignal™ West Dura Chemiluminescent Substrate and images were acquired using Gene Gnome from Syngene Bio-Imaging (CDD camera). The optical density of each band was quantified and normalized to the intensity of the calibration sample band using NIH ImageJ.

Circadian period length determination

Human skin fibroblasts and human glioma A172 cells transfected with the lentiviral circadian reporter mice *Bmal1*::luciferase (Brown et al., 2005, Gaspar and Brown, 2015) were plated in single culture dishes (35x10mm) at a cell density sufficient to reach 70-80% of confluency on the start day of recording of period length. After synchronization with dexamethasone (100 nM, 15 mins at 37°C), cells were cultured in DMEM (CM) supplemented with 10% heat-inactivated FBS, 10 mM HEPES and 0.1 mM luciferin. To determine the influence of ATP on circadian period length, CM was supplemented with glycolysis inhibitor (2-Deoxy-glucose, 4.5 g/L) and pyruvate (4 mM), or the cell cycle inhibitor AraC (100 μM). To further confirm the influence of ATP on molecular circadian clock, CM was supplemented with nutrient sensors inhibitors: compound C (1 μM), an AMPK inhibitor; Ex527 (1 μM), a selective inhibitor of SIRT1; AGK7 (1 μM), a selective inhibitor of SIRT3. To determine the role of Drp1-regulated mitochondrial bioenergetics, CM was supplemented with the inhibitor P110 (1 μM), a selective inhibitor of DRP1 or a mitochondrial division inhibitor or FK506 (1 μM), a calcineurin inhibitor. For at least 5 days, the amount of produced light that is proportional to Bmal1 gene expression was

measured using a Lumicycle instrument (Actimetrics). Data were analysed with Lumicycle Analysis software (Lumicycle™, version 2.31, Actimetrics Software) and the period of oscillation was calculated by least-mean-squares fitting of dampened sine wave functions to the actual data as described previously (Pagani et al., 2011).

Quantitative real-time PCR

Total RNA was extracted from lysates of synchronized fibroblasts using RNeasy Mini KIT (Qiagen). cDNA was generated using Ready-to-Go You-Prime First-Strand Beads (GE Healthcare). For data analysis, human *CDK4* was used as an endogenous control. Data are expressed as relative expression for each individual gene normalized to their corresponding controls. The primers used were purchased from Applied Biosystems and Microsynth (Probe ID: see Table S2). Data are expressed as relative expression for each individual gene normalized to their corresponding controls.

Quantification and statistical analysis

Data were presented as mean ± S.E.M. Graph Pad Prism 5.02 was used for statistical analysis and data presentation. The curves were generated by using a standard curve fit function in the GraphPad Prism software. For statistical comparisons, a Student's two-tailed t-test was used to compare single time points. Rhythmicity of metabolites and genes expression was assessed using an algorithm previously described for rhythmic transcripts.

The JTK-cycle algorithm was used as implemented in R by Kronauer as previously described (Dallmann et al., 2012). In brief, this algorithm characterizes samples as rhythmic or nonrhythmic using a nonparametric method based on a combination of the Jonckheere–Terpstra test for monotonic ordering and Kendall's τ test for association of measured quantities. Metabolites profiles were first crosschecked by visual inspection. Subsequently, the statistical significance of the circadian rhythmicity of each compound was evaluated with an independent permutation test to identify the false discovery rate for each metabolite. A window of 24 h was

used for the determination of circadian periodicity and a *P* value of <0.05 was considered as statistically significant.

Statistical parameters can be found in figure legends.

Supplemental table

Table S1, related to Figure 1: Complete list of all identified metabolites in serum-shocked U2OS.

All values are normalized (mean±SEM). Rhythmic compounds are indicated in red color. Abbr.: RI: retention index, HMDB: identification numbers of biochemicals in Human Metabolome Database, PT-p: p-values computed with the permutation test as described in Methods, Per: Period, LAG: peak phases, Amp: amplitude of oscillation, defined as the maximum divided by the minimum level of a particular biochemical in the first 24hrs of the experiment. Phase: Phase of the peak for rhythmic biochemicals.

Table S2: Primer sequences, related to STAR Methods section: "Quantitative real-time PCR".

Graphic Abstract

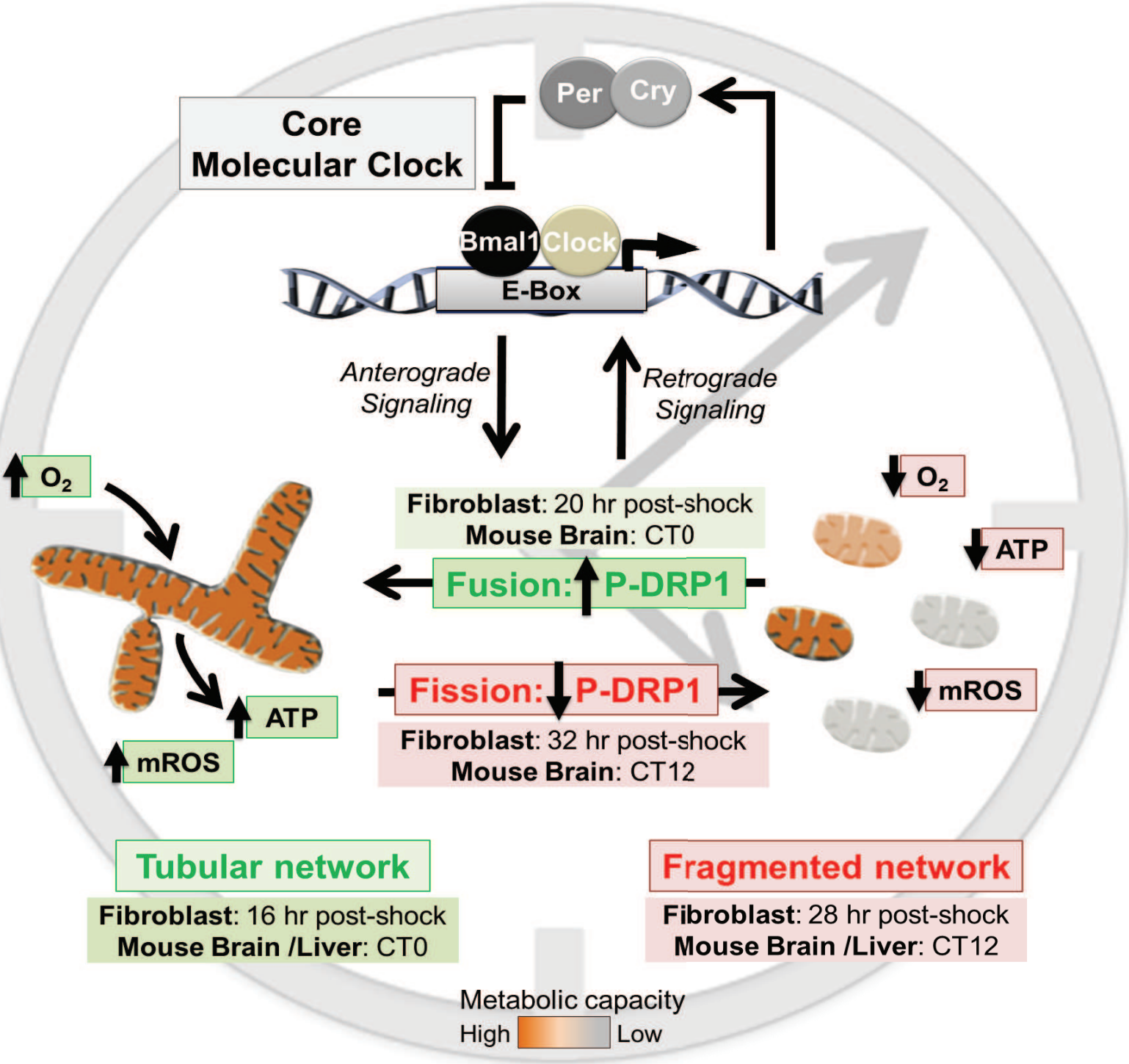

Figure 1

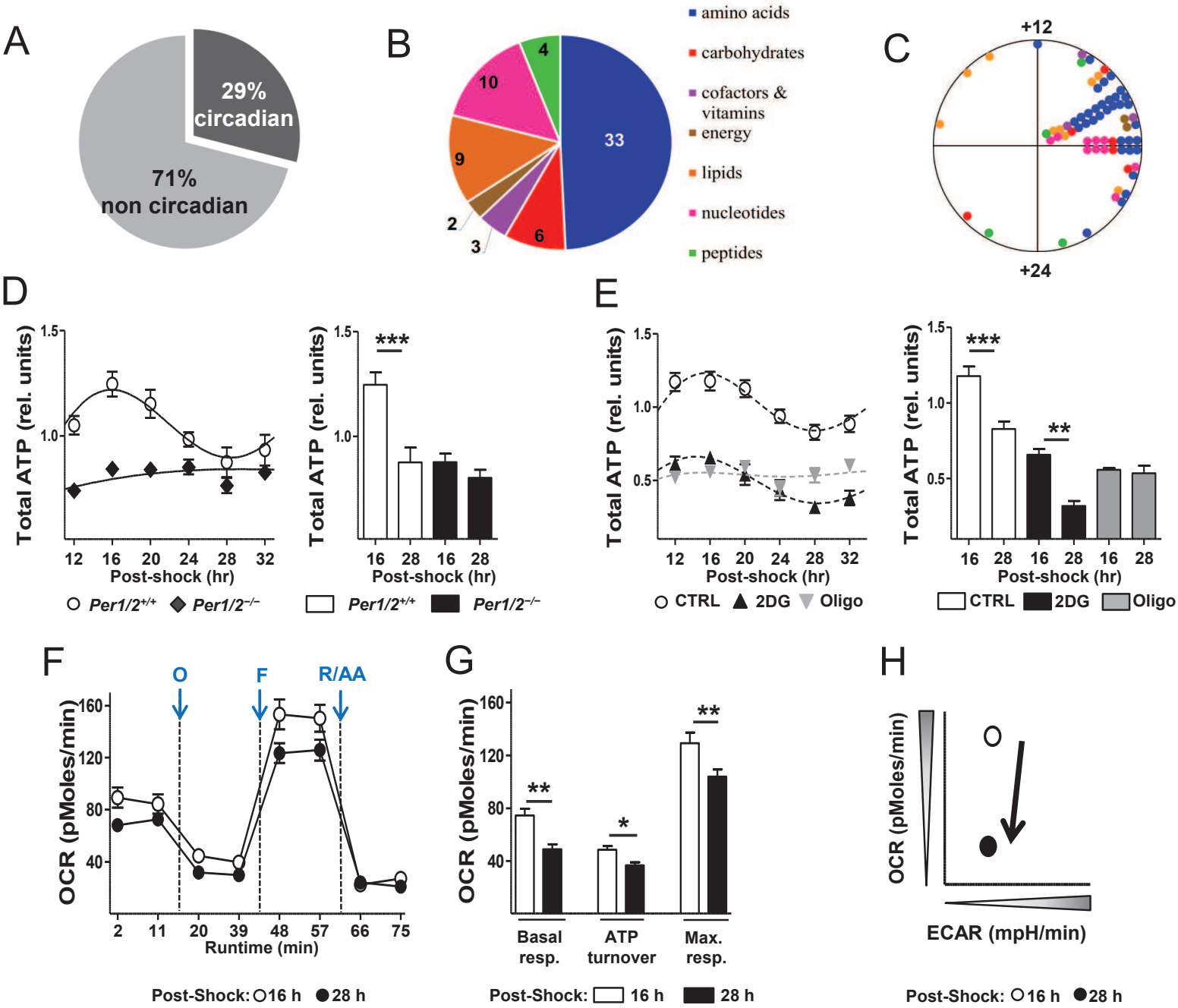
A
29%
circadian
71%
non circadian
B
amino acids
carbohydrates
cofactors & vitamins
energy
lipids
nucleotides
peptides
33
6
3
2
9
10
4
C
+12
+24
D
Total ATP (rel. units)
Post-shock (hr)
Per1/2+/+
Per1/2−/−
***
E
CTRL
2DG
Oligo
**
F
O
F
R/AA
OCR (pMoles/min)
Runtime (min)
Post-Shock: 16 h 28 h
G
Basal resp.
ATP turnover
Max. resp.
*
H
ECAR (mpH/min)

Figure 2

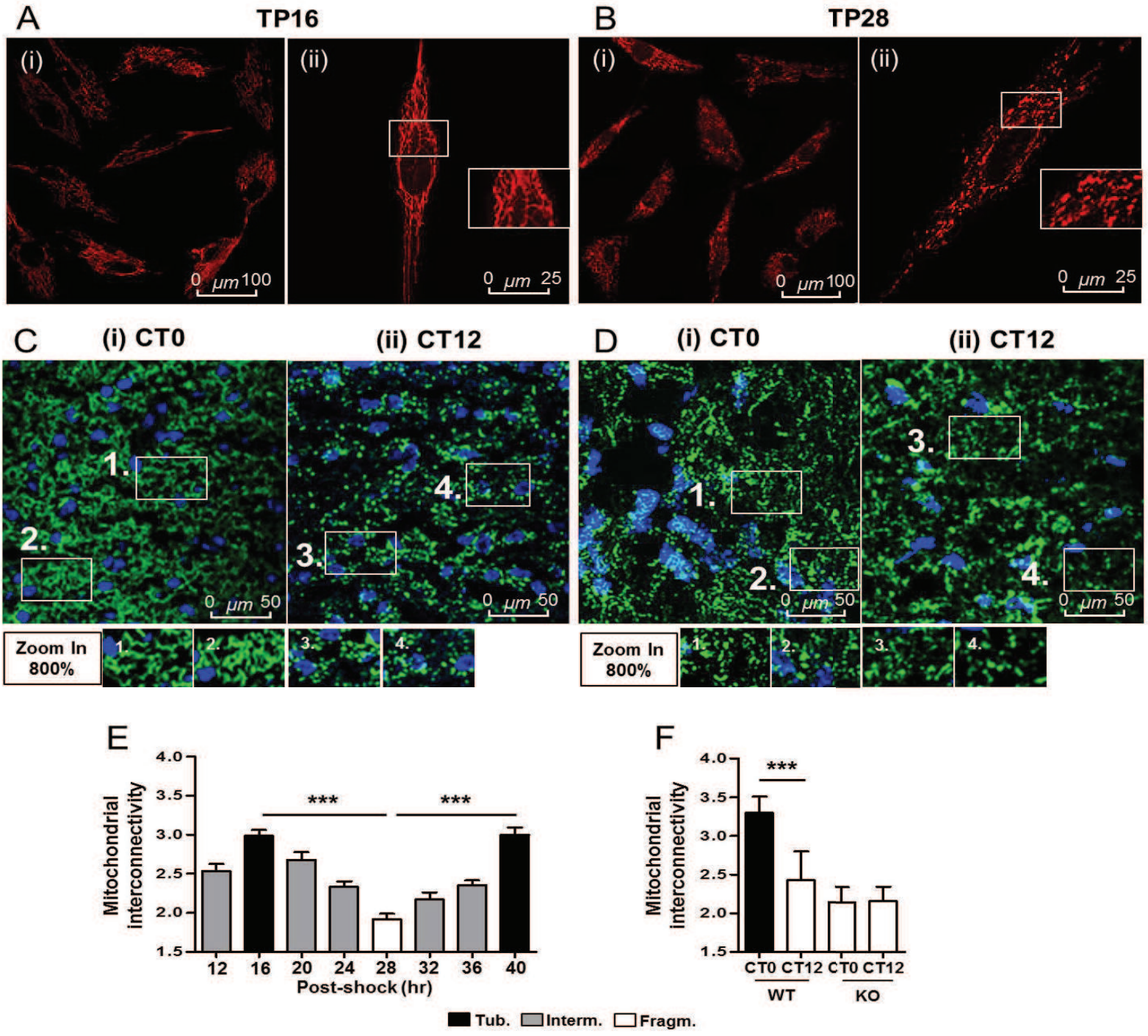
A
TP16
(i)
(ii)
0 μm 100
0 μm 25
B
TP28
(i)
(ii)
0 μm 100
0 μm 25
C
(i) CT0
(ii) CT12
1.
2.
3.
4.
0 μm 50
Zoom In 800%
D
(i) CT0
(ii) CT12
1.
2.
3.
4.
0 μm 50
Zoom In 800%
E
Mitochondrial interconnectivity
4.0
3.5
3.0
2.5
2.0
1.5
***
***
12 16 20 24 28 32 36 40
Post-shock (hr)
F
Mitochondrial interconnectivity
***
CT0 CT12 CT0 CT12
WT
KO
Tub.
Interm.
Fragm.

Figure 3

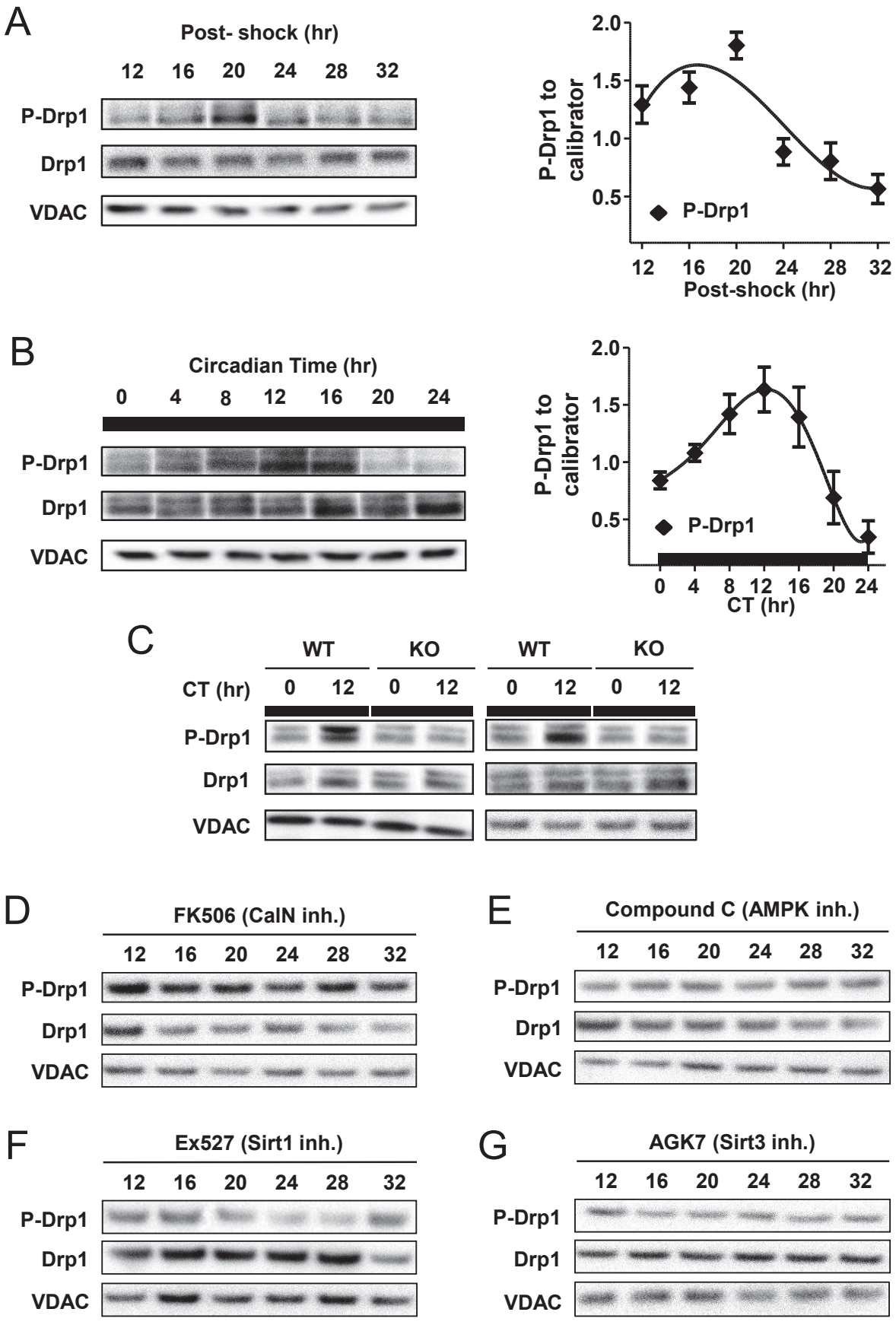
A
Post- shock (hr)
12 16 20 24 28 32
P-Drp1
Drp1
VDAC
P-Drp1 to calibrator
2.0
1.5
1.0
0.5
P-Drp1
12 16 20 24 28 32
Post-shock (hr)
B
Circadian Time (hr)
0 4 8 12 16 20 24
P-Drp1
Drp1
VDAC
P-Drp1 to calibrator
2.0
1.5
1.0
0.5
P-Drp1
0 4 8 12 16 20 24
CT (hr)
C
WT KO WT KO
CT (hr) 0 12 0 12 0 12 0 12
P-Drp1
Drp1
VDAC
D
FK506 (CaIN inh.)
12 16 20 24 28 32
P-Drp1
Drp1
VDAC
E
Compound C (AMPK inh.)
12 16 20 24 28 32
P-Drp1
Drp1
VDAC
F
Ex527 (Sirt1 inh.)
12 16 20 24 28 32
P-Drp1
Drp1
VDAC
G
AGK7 (Sirt3 inh.)
12 16 20 24 28 32
P-Drp1
Drp1
VDAC

Figure 4

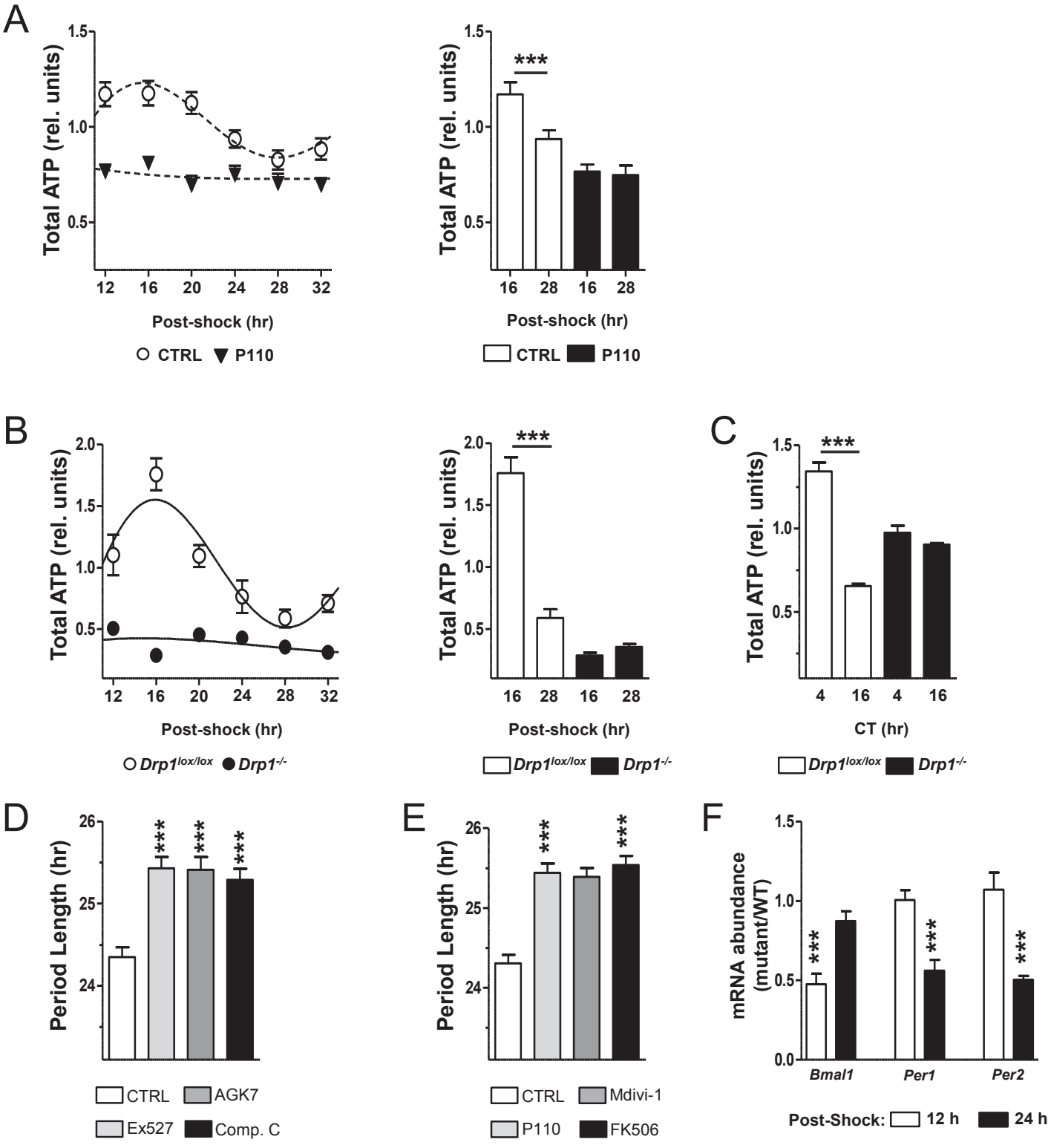
A
Total ATP (rel. units)
1.5
1.0
0.5
12 16 20 24 28 32
Post-shock (hr)
CTRL P110
***
16 28 16 28
Post-shock (hr)
CTRL P110
B
Total ATP (rel. units)
2.0
1.5
1.0
0.5
12 16 20 24 28 32
Post-shock (hr)
Drp1lox/lox Drp1-/-
***
16 28 16 28
Post-shock (hr)
Drp1lox/lox Drp1-/-
C
Total ATP (rel. units)
***
4 16 4 16
CT (hr)
Drp1lox/lox Drp1-/-
D
Period Length (hr)
26
25
24
***
CTRL AGK7
Ex527 Comp. C
E
Period Length (hr)
26
25
24
***
CTRL Mdivi-1
P110 FK506
F
mRNA abundance (mutant/WT)
1.5
1.0
0.5
0.0
***
Bmal1 Per1 Per2
Post-Shock: 12 h 24 h

Supplemental Information

Circadian control of DRP1 activity regulates mitochondrial dynamics and bioenergetics.

Karen Schmitt, Amandine Grimm, Robert Dallmann, Bjoern Oettinghaus, Lisa Michelle Restelli, Melissa Witzig, Naotada Ishihara, Katsuyoshi Mihara, Jürgen A Ripperger, Urs Albrecht, Stephan Frank, Steven A. Brown, Anne Eckert

Supplementary figure titles and legends

Figure S1, related to Figure 1

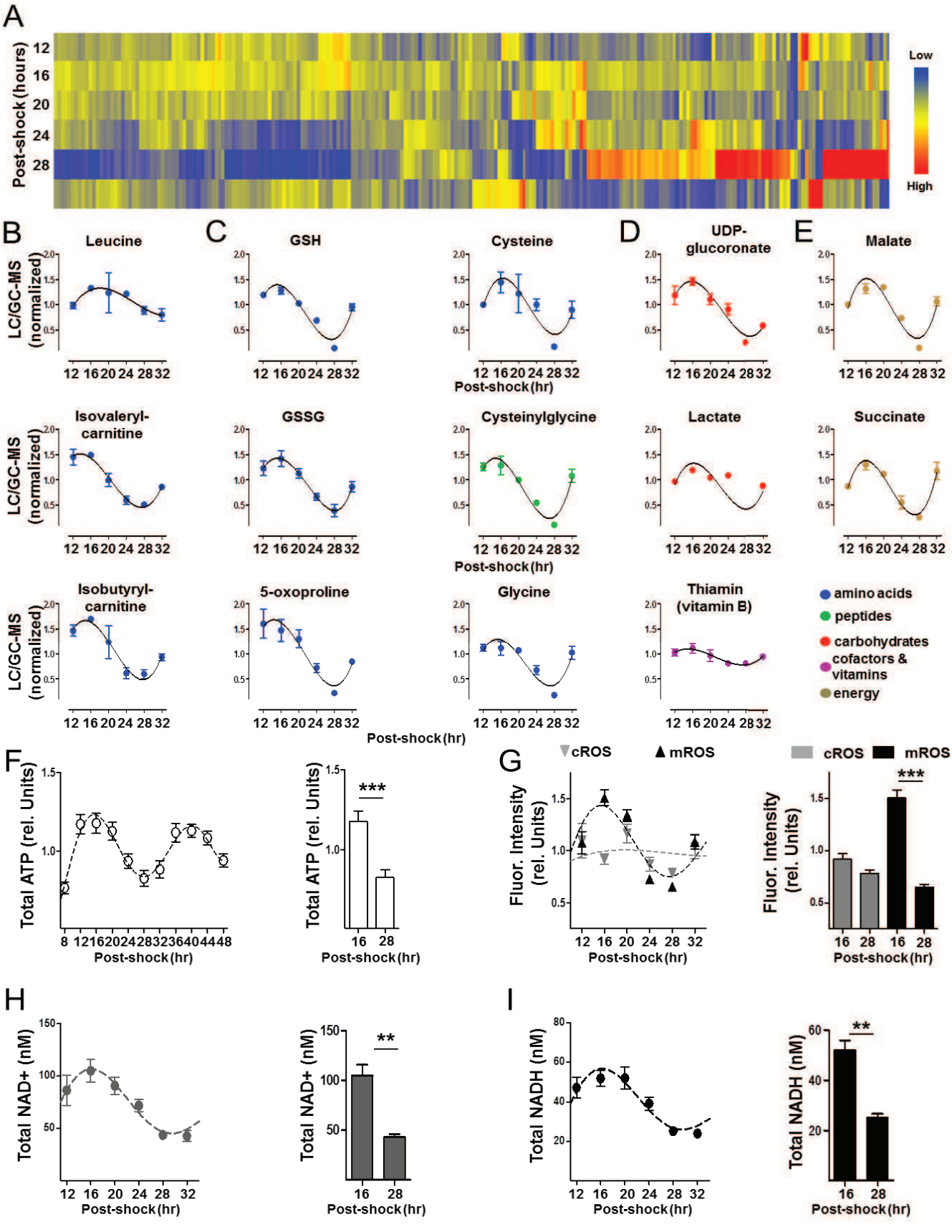

(**A**) Heat plots for all identified metabolites in synchronized human U2OS cells.

(**B-E**) Accumulation profiles of oscillating metabolites involved in branched-chain amino acid metabolism (**B**), GSH/GSSG metabolism (**C**), glycolysis (**D**), and TCA cycle (**E**), presented as mean ± SEM. Raw peak values for all metabolites were normalized to have a median of 1.

(**F**) Relative total ATP levels from serum-shocked human skin fibroblasts measured at the indicated time points (JTK_Cycle, $P=1.78*10^{-15}$). Right panel displays relative total ATP level at 16 hours post-shock (peak of ATP content) and at 28 hours (trough of ATP content).

(**G**) Cytosolic (cROS) and mitochondrial (mROS) reactive oxygen species levels were evaluated in serum-shocked human skin fibroblasts (JTK_Cycle, P_{mROS}=5.40*10-21, P_{cROS}=0.489). Right panel displays cROS and mROS levels at 16 hours post-shock (peak) and at 28 hours (trough)

(**H**) Total NAD^+ content assessed from brain of non-fasted wild-type mice kept in constant darkness every 4 hours for 24 hours (JTK_Cycle, $P=1.23*10^{-6}$). Right panel displays relative total NAD^+ level at CT4 (peak) and at CT16 (trough)).

(**I**) Total NADH content from brain of non-fasted wild-type mice kept in constant darkness, assessed every 4 hours for 24 hours (JTK_Cycle, P=0.000168). Right panel displays relative total NAD^+ level at CT4 (peak) and at CT16 (trough)

All data are represented as mean ± SEM of at least three independent samples (n = 4 or 6 per time point) (**F-I**). **P<0.01, ***P < 0.001 for Student's two-tailed t-test comparing time points (e.g. 16h versus 28h).

Figure S2, related to Figure 1 & 2

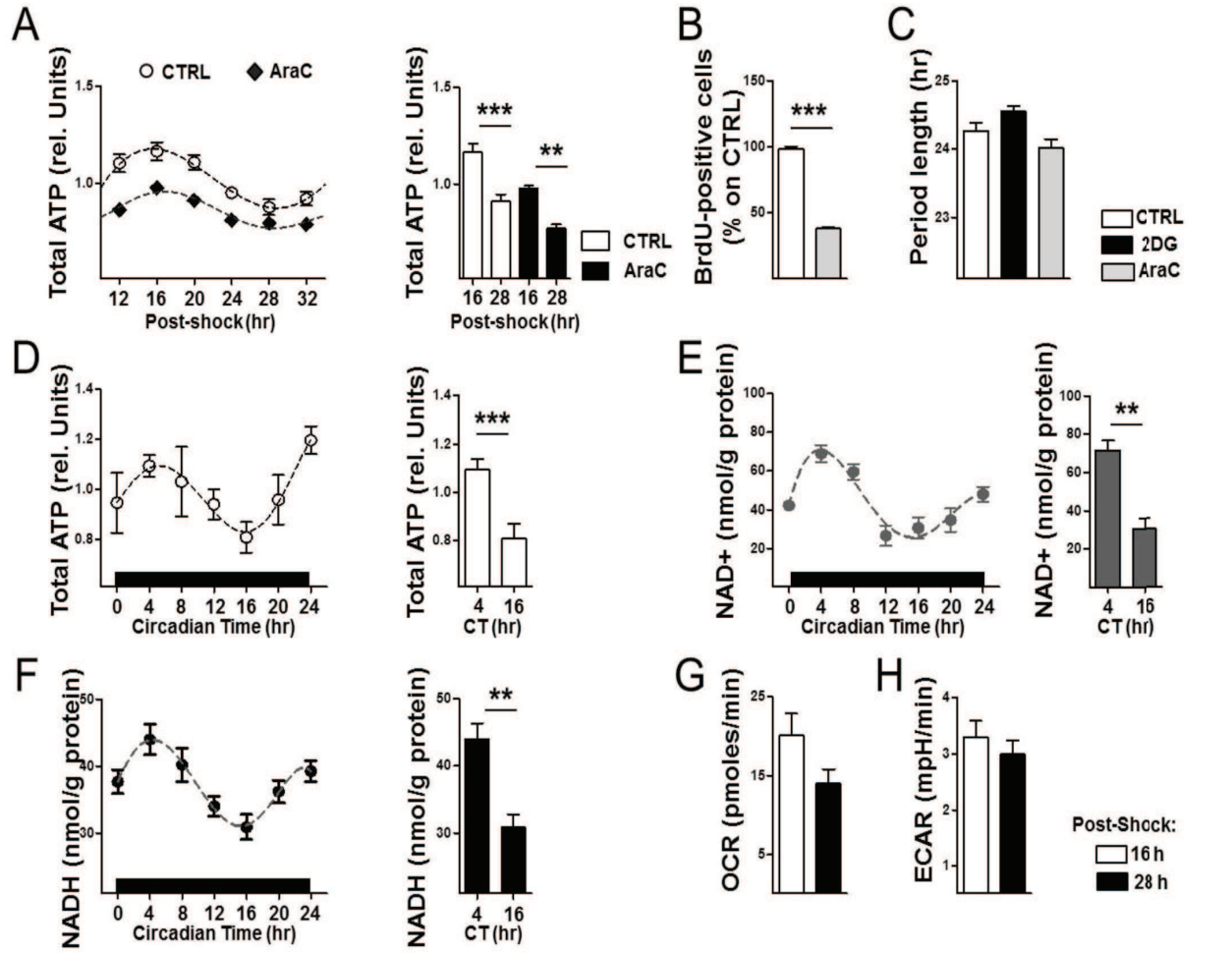

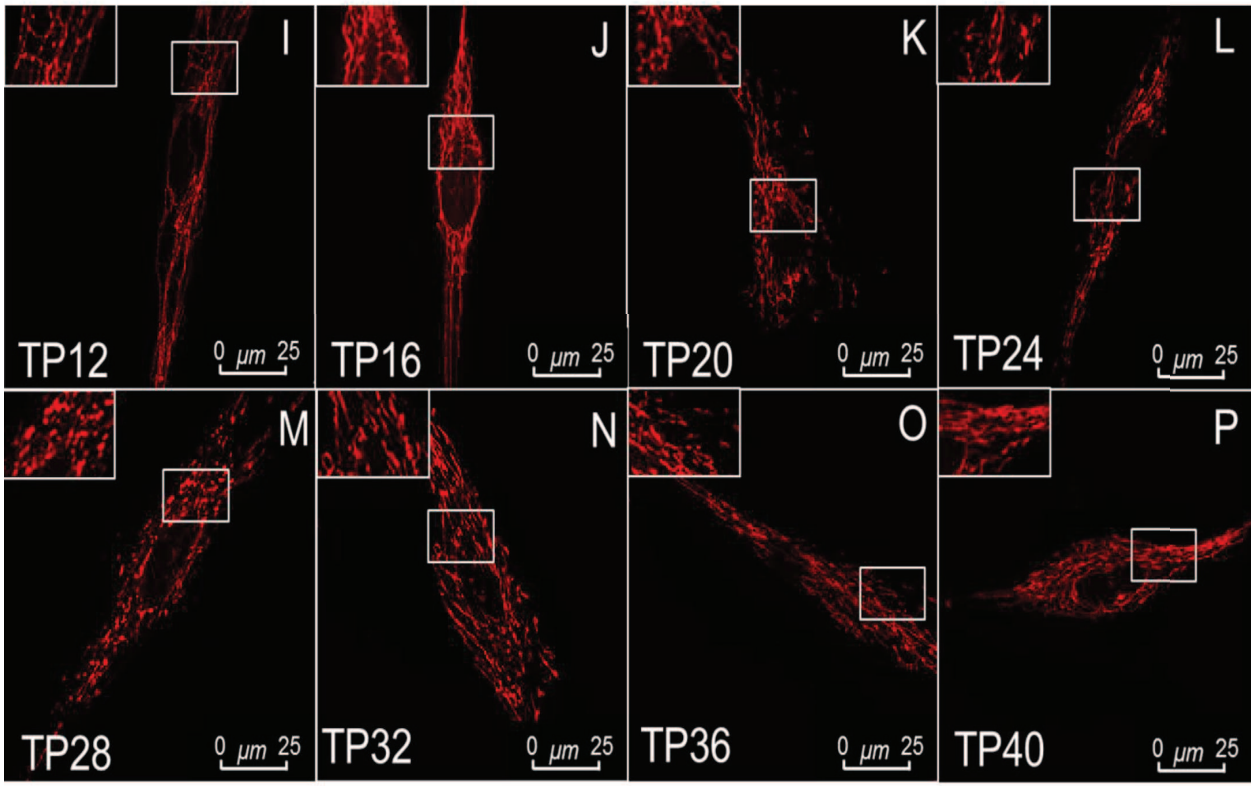

(A) Left panel, relative total ATP contents from serum-shocked human skin fibroblasts treated with cytosine β-D-arabinofuranoside (AraC, 100 μM) compared to non-treated cells (CTRL) measured at the indicated time points in cells (n=6 per time point, JTK_Cycle, $P_{CTRL}=4.69*10^{-12}$, $P_{AraC}=3.0*10^{-10}$). Right panel displays relative total ATP level at 16 hours post-shock (peak of ATP content) and at 28 hours (trough of ATP content) in control and treated conditions).

(**B**) Percentage of BrdU- positive cells in absence and presence of AraC at 24 hours post-shock.

All data are represented as mean ± SEM of at least three independent samples (n = 4 or 6 per time point) (**A, B**). **P<0.01, ***P < 0.001 for Student's two-tailed t-test comparing single time points between CTRL and treated cells.

(**C**) Circadian period length determined in dexamethasone - synchronized human skin fibroblasts transfected with Bmal1::luciferase reporter in presence of 2 deoxy-glucose (4.5 g/L) and AraC (100 μM) compared to control (CRTL).

(**D**) Left panel shows relative total ATP levels measured in brain of wild-type mice kept in constant darkness (WT Brain) every 4 hours for 24 hours (7 time points, n=4 for each, JTK_Cycle, P=0.0077). Right panel displays relative total ATP level at circadian time 4 (CT4; peak of ATP content) and 16 (CT16; trough of ATP content) ().

(**E**) Total NAD^+ measured in serum-shocked human skin fibroblasts at the indicated time points (6 time points, n=6 for each, JTK_Cycle, $P=2.18*10^{-8}$). Right panel displays relative total NAD^+ level at 16 hours post-shock (peak) and at 28 hours (trough)).

(**F**) Total NADH measured in serum-shocked human skin fibroblasts at the indicated time points (6 time points, n=6 for each, JTK_Cycle, $P=6.68*10^{-5}$). Right panel displays relative total NAD^+ level at 16 hours post-shock (peak) and at 28 hours (trough)).

All data are represented as mean ± SEM (**D-F**). **P<0.01, ***P < 0.001 for Student's two-tailed t-test comparing single time points (16 versus 28 hours).

(**G**) OCR related to the proton leak (independent to ATP production) at 16 hours post-shock and 28 hours post-shock in human skin fibroblast.

(**H**) Extracellular Acidification Rate (ECAR) corresponding to glycolytic rate at 16 hours post-shock and 28 hours post-shock in human skin fibroblast.

All data are represented as mean ± SEM of three independent samples (n= 11 per time point).

(**I-P**) Mitochondrial network morphology assessed at 4 hours intervals for 8 time points in synchronized fibroblasts (**I, K, L, N, O**) Intermediate network; (**J, P**) Tubular network; (**M**) Fragmented network. For each representative image, a zoom-in image is provided (400%). Scale bar = 25 μm.

Figure S3, related to Figure 2

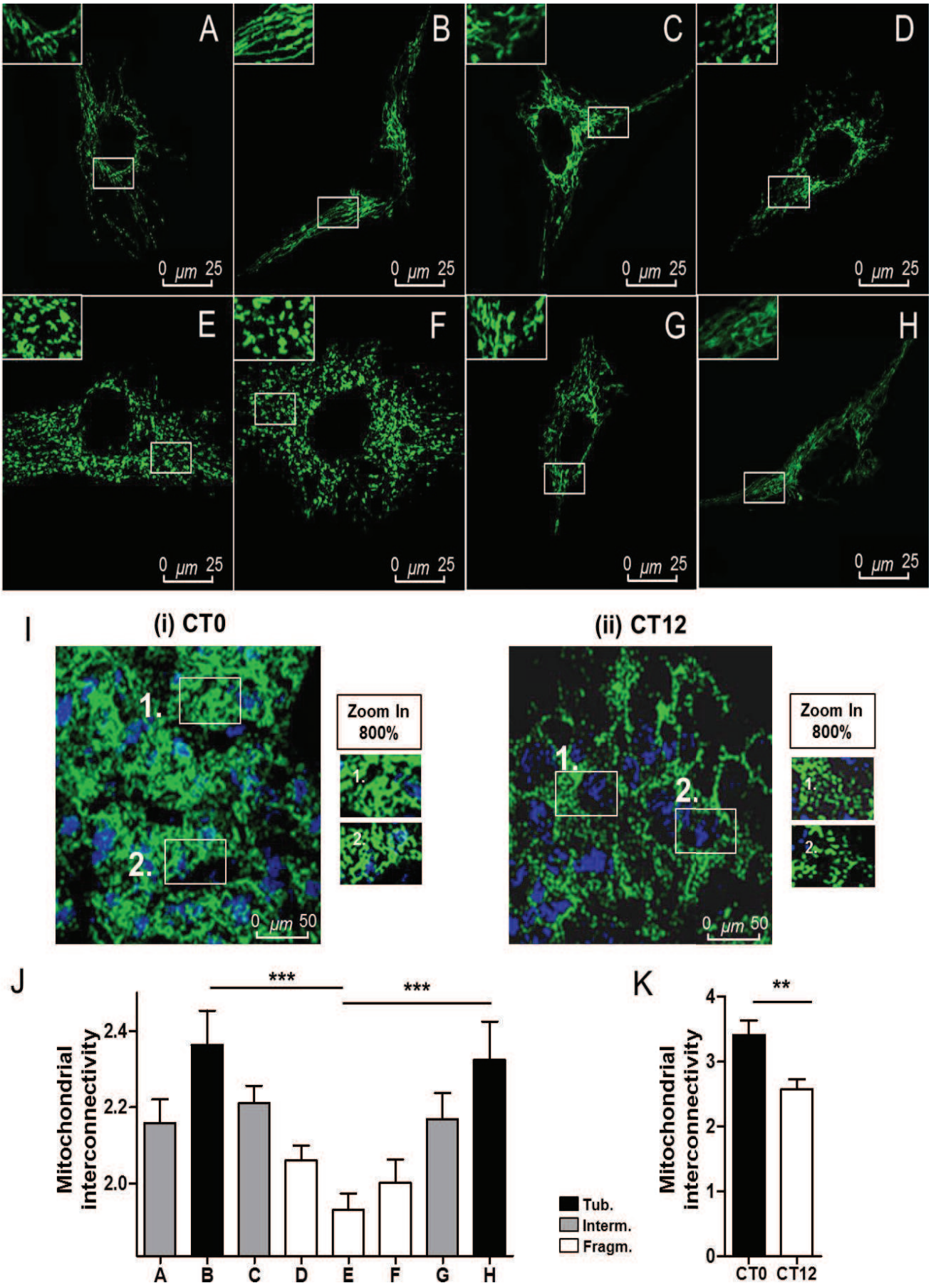

(**A-H**) Mitochondrial network morphology assessed at 4 hours intervals for 8 time points in synchronized A172 glioma cells transfected with a GFP plasmid containing a mitochondrial targeting sequence. (**A, C, G**) Intermediate network; (**B, H**) Tubular network; (**D, E, F**) Fragmented network. For each representative image, a zoom-in image is provided (400%). Scale bar = 25 μm.

(**I**) Mitochondrial network morphology assessed in liver sections from non-fasted wild-type mice kept in darkness condition at CT0 (i) and CT12 (ii). Scale bar = 50 μm.

(**J**) Quantification of mitochondrial interconnectivity corresponding to the conditions A to H. On average 10`000-20`000 mitochondrial organelles were analyzed per time point (n = 25-30 images per time point; JTK_Cycle, P = 0.000607).

(**K**) Quantification of mitochondrial interconnectivity at CT0 and CT12 (n=6 sections per condition,). On average 2`500-8`500 mitochondrial units were analyzed per time point.

Data are represented as average ± SEM (**J, K**). ***P<0.001 for Student's two-tailed t test comparing single time points.

Figure S4, related to figure 4

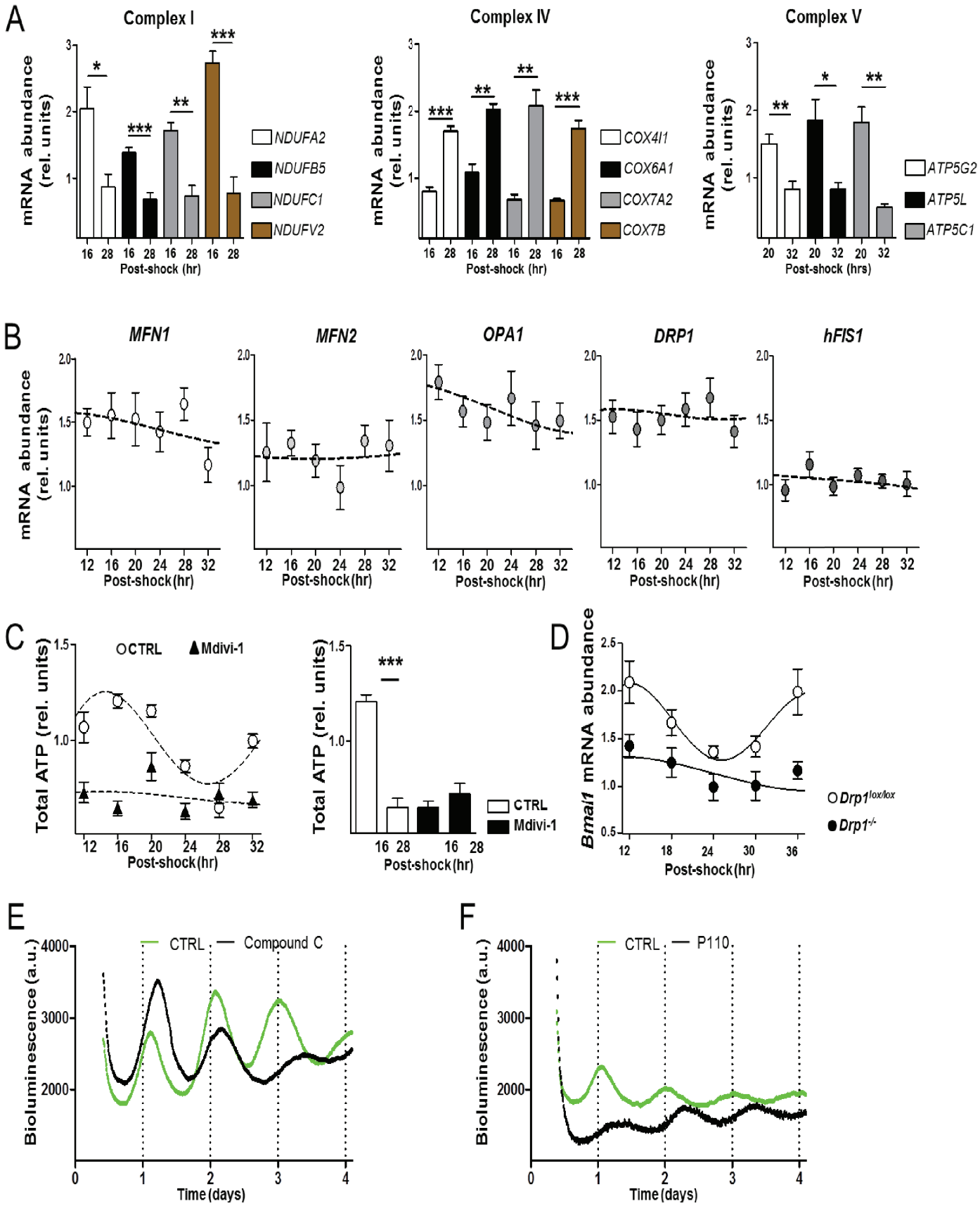

(**A**) Relative mRNA expression of complex I, IV and V subunits at 16 hours post-shock (corresponding to the peak in gene expression) and 28 hours post-shock (corresponding to the trough in gene expression) (JTK_Cycle, $P_{NDUFA2}=3.96*10^{-5}$, $P_{NDUFB5}=8.57*10^{-6}$, $P_{NDUFC1}=4.88*10^{-15}$, and $P_{NDUFV2}=7.61*10^{-5}$).

(**B**) Profile of relative mRNA expression of nuclearly-encoded genes related to mitochondrial fusion (*MFN1*, *MFN2* and *OPA1*) and mitochondrial fission (*DRP1* and h*FIS1*) in serum-shocked human skin fibroblasts (JTK_Cycle, $P_{MFN1}=0.809$, $P_{MFN2}=0.426$, $P_{OPA1}=0.175$, $P_{DRP1}=0.215$, $P_{hFIS1}=0.827$).

(**C**) Left panel, relative total ATP levels from serum-shocked human skin fibroblasts treated with Mdivi-1 (50 μM) compared to non-treated cells (CTRL) measured at the indicated time points (n=6 per time point, JTK_Cycle, P_{CTRL}=5.36*10-20, $P_{Mdivi-1}=0.8581$). Right panel, relative total ATP level at 16 hours post-shock (peak of ATP content) and at 28 hours (trough of ATP content) in control and treated conditions.

All data are represented as mean ± SEM of at least three independent samples (n=6 per time point,) (**A- C**). *P<0.05, **P<0.01, ***P<0.001 for Student's two-tailed t test comparing single time points (**A, B**) or comparing single time points between CTRL and treated cells (**C**).

(D) Relative mRNA expression of *Bmal1* evaluated from in *Drp1* $^{-/-}$ MEFs compared to *Drp1*$^{lox/lox}$ MEFs at 12, 18, 24, 30 and 36 hours post-shock (n=6 per time point, JTK_Cycle, $P_{Drp1^{lox/lox}}=0.000951$, $P_{Drp1^{-/-}}=0.864$).

(E, F) Representative bioluminescence records determined in dexamethasone - synchronized human skin fibroblasts transfected with *Bmal1*::luciferase reporter in presence of (**E**) an AMPK inhibitor (compound C, 1 μM) and (**F**) a DRP1 inhibitor, P110 (1 μM), compared to control (CTRL) (n = 3).

Table S2: Primer sequences, related to STAR Methods section: "Quantitative real-time PCR".

	Primer	Probe ID (Applied Biosystems)
Fusion	*MFN1*	Hs00250475_m1
	MFN2	Hs00208382_m1
	OPA1	Hs00323399_m1
Fission	*DRP1*	Hs00247147_m1
	FIS1	Hs00211420_m1
OXPHOS	*NDUFA2* (complex I)	Hs00159575_m1
	NDUFB5 (complex I)	Hs00159582_m1
	NDUFC1 (complex I)	Hs00159587_m1
	NDUFV2 (complex I)	Hs00221478_m1
	COX4I1 (complex IV)	Hs00971639_m1
	COX6A1 (complex IV)	Hs01924685_g1
	COX7A2 (complex IV)	Hs01652418_m1
	COX7B (complex IV)	Hs00371307_m1
	ATP5G2 (ATP synthase)	Hs01096582_m1
	ATP5C1 (ATP synthase)	Hs01101219_g1
	ATP5L (ATP synthase)	Hs00758883_s1

Primer	Sequence (Microsynth)
BMAL1	forward, 5'-GAAGACAACGAACCAGACAATGAG-3'
	reverse, 5'-ACATGAGAATGCAGTCGTCCAA-3'
	probe, 5'-Yakima Yellow-TGTAACCTCAGCTGCCTCGTCGCA-BHQ1-3'
PER1	forward, 5'-CGCCTAACCCCGTATGTGA-3'
	reverse, 5'-CGCGTAGTGAAAATCCTCTTGTC-3'
	probe, 5'-Yakima Yellow-CGCATCCATTCGGGTTACGAAGCTC-BHQ1-3'
PER2	forward, 5'-GGGCAGCCTTTCGACTATTCT-3'
	reverse, 5'-GCTGGTGTCCAACGTGATGTACT-3'
	5'-Yakima Yellow-CATTCGGTTTCGCGCCCGGG-BHQ1-3'

KEY RESOURCES TABLE

REAGENT or RESOURCE	SOURCE	IDENTIFIER
Antibodies		
DRP1 (D6C7) Rabbit mAb	Cell Signaling Technology	Cat# 8570S, RRID:AB_10950498
Phospho-DRP1 (Ser637) Antibody	Cell Signaling Technology	Cat# 4867S, RRID:AB_10622027
VDAC Antibody	Cell Signaling Technology	Cat# 4866, RRID:AB_2272627
Bacterial and Virus Strains		
Biological Samples		
Chemicals, Peptides, and Recombinant Proteins		
Dexamethasone	Sigma-Aldrich	Cat#D1756; CAS: 50-02-2
Cytosine β-D-arabinofuranoside hydrochloride (AraC)	Sigma-Aldrich	Cat#C6645; CAS: 69-74-9
2-deoxy-D-glucose	Sigma-Aldrich	Cat#D6134; CAS: 154-17-6
2',7'-Dichlorofuorescin diacetate	Sigma-Aldrich	D6883; CAS: 4091-99-0
Dihydrorhodamine-123	Sigma-Aldrich	D1054; CAS: 109244-58-8
P110 (H - YGR KKR RQR RRG GDL LPR GS - NH2 (20AA))	Eurogentec (Qi et al, 2013)	Peptide Custom Synthesis
Mdivi-1 (Drp1 inhibitor)	Sigma-Aldrich	Cat#M0199; CAS: 338967-87-6
MitoSOX™ Red Mitochondrial Superoxide Indicator, for live-cell imaging	ThermoFisher Scientific	Cat#M36008
Mitotracker Red CMX ROS	ThermoFisher Scientific	Cat#M7512; CAS: 167095-09-2
To-PRO-3 iode	ThermoFisher Scientific	Cat#T3605; CAS: 157199-63-8
DyNamo ColorFlash Probe qPCR Kit	ThermoFisher Scientific	Cat#456L
SuperSignal West Dura Chemiluminescent Substrate	ThermoFisher Scientific	Cat#34075
Lipofectamine 2000 Transfection Reagent	ThermoFisher Scientific	Cat#11668019
Compound C (BML-275; AMPK inhibitor)	Enzo Life Sciences	Cat#BML-El369; CAS: 866405-64-3
AGK7 (Sirt3 inhibitor)	Enzo Life Sciences	Cat#ENZ-CHM146; CAS: 304896-21-7
FK506 (Calcineurin inhibitor)	Enzo Life Sciences	Cat#ALX-380-008; CAS: 104987-11-3
Ex527 (Selisistat; Sirt1 inhibitor)	Selleck Chemicals	Cat#S1541; CAS: 49843-98-3
Critical Commercial Assays		

Vialight TM Plus Cell Proliferation and Cytotoxicity BioAssay Kit	Lonza	Cat#LT07-321
Seahorse XF FluxPak	Agilent Seahorse XF Technology	Cat#100850-001
Seahorse XF Cell Mito Stress Test Kit	Agilent Seahorse XF Technology	Cat#103015-100
BrdU Cell Proliferation Assay	Merk Millipore	Cat#QIQ58
RNeasy Mini KIT	Qiagen	Cat#74104
Ready-To-Go You-Prime First-Strand Beads	GE Healthcare Life Sciences	Cat#27-9264-01
ProLong® Gold antifade reagent	ThermoFisher Scientific	Cat#P36930
Deposited Data		
Experimental Models: Cell Lines		
Human: primary skin fibroblasts	Isolated from subjects (Pagani et al.,2011)	N/A
Human: osteosarcoma U2OS cell line	The Brown Laboratory	RRID:CVCL_0042
Human: glioma A172 cell line	The Brown Laboratory	RRID:CVCL_0131
Mouse: Drp1lox/lox and Drp1-/- mouse embryonic fibroblasts	The Ishihara and Mihara Laboratories	
Mouse: mPer1/mPer2+/+ and-/- mouse embryonic fibroblasts	The Albrecht Laboratory	
Experimental Models: Organisms/Strains		
Mouse: Drp1 flx/flx and Drp1 flx/flx CreERT2 C57BL/6J	The Ishihara and Mihara Laboratories	Ishihara et al., 2009
Mouse: mPer1/mPer2 +/+ and mPer1/mPer2 -/- C57BL/6J	The Albrecht Laboratory	Zheng et al., 2001
Oligonucleotides		
Primers for mitochondrial fusion/fission, please see Table S2	This paper	N/A
Primers for OxPhos subunits, please see Table S2	This paper	N/A
Primers for clock genes, please see Table S2	This paper	N/A
Recombinant DNA		
pABpuro-BluF (luciferase reporter for BmalI promoter)	Brown et al., 2005	Addgene Plasmid, Cat#46824
pEGFP-N1-mt-ro2GFP (gift from S. James Remington)	Hanson et al.,2004	Addgene Plasmid, Cat#82408
Software and Algorithms		
Prism Version 5.02	GraphPad	https://www.graphpad.com/scientific-software/prism/
ImageJ	NIH	https://imagej.nih.gov/ij/
JTK-cycle algorithm	Dallmann et al. 2012	http://www.openwetware.org/wiki/HughesLab:JTK_Cycle
Other		